



Research master's degree 2 : Earth, Planets and Environmental Sciences

Geosciences Courses - University year 2019-2020

Master thesis

**Geophysical signature of the alpine slab: Field analogues
and direct models**

Submitted and argued by Manon SONNET

Under the direction of Loïc Labrousse¹, Jérôme Bascou² and Alexis Plunder³

1. Laboratory ISTeP (Paris Institute of Earth Sciences) - Sorbonne University.
2. Laboratory LMV (Magmas and Volcanoes) - Saint Etienne University.
3. BRGM (Geological and Mining Research Office), Orléans

July 2020



Table of contents

Abstract	4
Résumé	4
I. Introduction	5
A. Seismic imaging of the lower crust in mountain belts	5
B. Eclogitization from a petrophysical perspective	6
C. The alpine slab : geological context and geophysical signature	7
II. State of the art	8
A. Advances in geophysics	8
B. Progress on the seismic properties of the rocks	8
C. The help of numerical models : bring the gap in the scale transfer	9
III. Approach and results	10
A. Sampling	12
B. Methods	13
1. Bulk rock chemistry	13
2. Thermodynamic and seismic properties modeling	15
3. Lattice Preferred Orientations	15
C. Results	16
1. From bulk chemistry to PT velocity map	16
a) Major element composition of bulk-rock samples	16
b) Thermodynamic modeling	19
c) Seismic properties modeling from mineral proportions	20
2. From LPO to velocity tensors	22
a) Crystallographic orientations	22
b) Seismic properties modeling from fabric	23
IV. Discussion	24
A. Comparative impact of fabric and mineralogical proportions on seismic properties	24
1. The unmodified crust scenario	24
2. The fully equilibrated crust at depth scenario	26
B. What is the petrological sensitivity of geophysical images?	27
C. What next? Synthetics geophysical signature of hecto- to kilometer scale structures	27
V. Conclusion	28
VI. Acknowledgments	28
VII. References	29
VIII. Appendix 1 - Hackers, QAFP and AFM diagrams	32

List of tables and figures

I. Introduction

Figure 1 - Unravelling of the alpine slab structure by seismic imaging over the years.	5
Figure 2 - Tectonic map of the Western Alps.	7
Figure 3 - CCP depth sections computed for events with different ranges of back-azimuth.	8
Figure 4 - Seismic properties of alpine eclogite samples.	9

II. State of the art

Figure 5 - Sampling spot map.	10
Table 1 - Synthesis of the sample locations and nature of the rock.	11
Table 2 - Synthesis of microscopic observations for each sample.	12
Figure 6 - Microscopic photo of thin sections.	14

III. Approach and results

Figure 7 - Principle of the transmission Kikuchi diffraction used for EBSD analysis.	15
Table 3 - Results of ICP-MS measurements on 18 samples.	17
Figure 8 - TAS diagram and FeO/(FeO+MgO) Harker diagram.	18
Figure 9 - Pseudosections from Theriak-Domino.	19
Figure 10 - Results of seismic velocities modeling (V_p , V_s and V_p/V_s ratio).	20
Figure 11 - Phases maps of 3 on 4 samples analyzed via EBSD.	23
Figure 12 - Synthesis of V_p and anisotrope modeling via MTEX.	25

IV. Discussion

Figure 13 - Variations of V_p with depth along the alpine slab.	26
Figure 14 - Complexity of the nature and structure of a rock in comparison with tomographic images.	27

Appendix 1 - Hackers, QAFF and AFM diagrams	32
---	----

Abstract

Recent geophysical data (receiver functions and volume wave tomography) in the Alps show the continuity of the Alpine dipping panel with the lower continental crust of the European plate. The eclogitization of the continental crust is often mentioned to explain its signature and its « loss ». The aim of the present study is to use analogous potentials in the field of this European crust, to directly predict the seismic properties of the buried crust. Here, we focus on the basic intercalations present in the Hercynian basement series of the external crystalline massifs.

Base on the bulk rock chemistries of the samples, pressure-temperature velocity diagrams can be calculated on the assumption that the rocks have completely rebalanced during burial. The garnet and omphacite stability are the major contrast for all the chemistry studied. From the fabric rocks, determined by EBSD analyses, the anisotropy of the volume wave velocity tensors can be partially reconstructed and shows that the amphibole content of the rocks is the first factor controlling their anisotropy signature. In a hypothetical possibility where the selected rocks are relevant analogues, we compared the evolution of the seismic properties according to the possible thermal gradients with the effective P-wave velocity profile at the top of the Alpine dipping panel. This suggests that it reacted only slightly to the thermal rebalancing of the collision prism. So that it kept the imprint of its burial along a cold gradient.

Résumé

Les données récentes de géophysique (fonctions-récepteurs et tomographies en ondes de volume) dans les Alpes montrent la continuité du panneau plongeant alpin avec la croûte continentale inférieure de la plaque Européenne. L'éclogitisation de la croûte continentale est souvent mentionnée pour expliquer sa signature et sa « disparition ».

La démarche de la présente étude est de partir de potentiels analogues de terrain du protolithe de cette croûte européenne, en l'occurrence les intercalations basiques présentes dans les séries de socle hercynien des massifs cristallins externes, pour prédire de manière directe les propriétés sismologiques de la croûte enfouie.

A partir des chimies des roches échantillonnées, des diagrammes de vitesse en pression température sont calculables en faisant l'hypothèse que les roches se sont totalement rééquilibrées lors de leur enfouissement. Les limites du champ à grenat et omphacite constituent le contraste majeur pour toutes les chimies étudiées. A partir des textures des roches, déterminées par analyses EBSD, l'anisotropie des tenseurs de vitesse des ondes de volume peut-être partiellement reconstituée, et montre que la teneur en amphiboles des roches est le premier facteur de contrôle de leur signature en anisotropie. Selon l'hypothèse d'école où les roches choisies sont des analogues pertinents, la comparaison des évolutions de propriétés théoriques selon les gradients thermiques possibles avec le profil de vitesse effectif des ondes P au sommet du panneau plongeant alpin laisse penser que celui-ci n'a que peu réagi au rééquilibrage thermique du prisme collisionnel. Il a gardé l'empreinte de son enfouissement le long d'un gradient froid.

I. Introduction

Subduction and collision zones are the major places for recycling the crust. This can either be re-injected into the mantle or integrated into an orogenic wedge. These processes take place on spatial and temporal scales beyond human reach and occur at extremely great depths, making observations complex. Thus, geophysical imaging techniques are widely used to study them (e.g. Rondenay et al., 2008, Schulte-Pelkum et al., 2005, Yuan et al., 2000).

Among these, the receiver function method is the most relevant to image velocity contrasts within the crust. Based on P wave conversion, this method is indeed more sensitive to contrasts and less to continuous absolute velocity changes within layers. Yet, the interpretation of these images is limited by their resolution and our knowledge of the seismic properties of rocks.

A. Seismic imaging of the lower crust in mountain belts

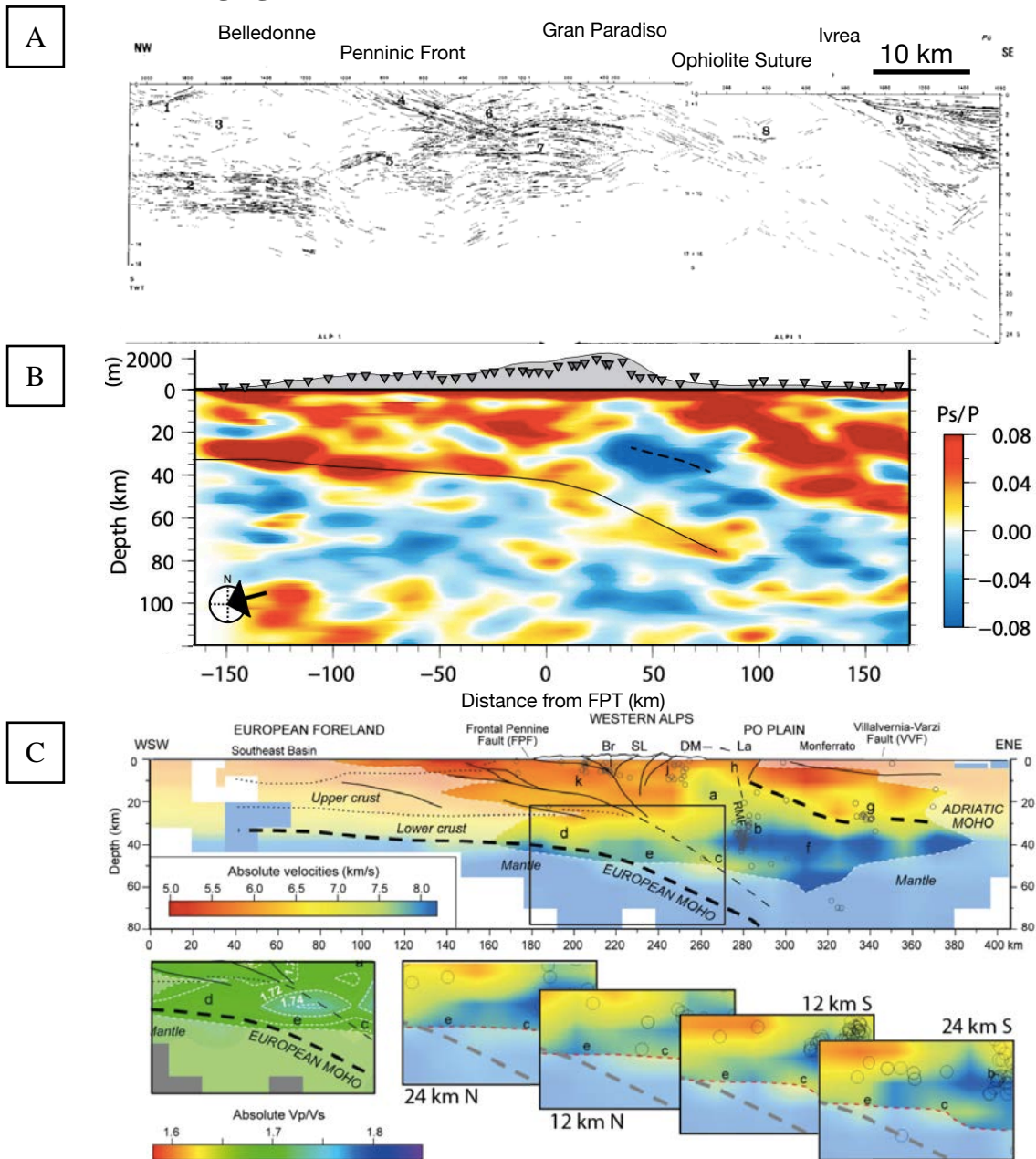


Figure 1: Unravelling of the alpine slab structure by seismic imaging over the years.

A. Vertical seismic reflection profile of the ECORS-CROP travers through the Western Alps. From Nicolas et al., 1990. B. Interpretation of the crustal-scale geological cross section from common conversion point depth section (Zhao et al. 2015). Continuous black line is the European Moho. Dashed black line is the inverted Moho. C. Slab signature in P-wave tomography and V_p/V_s ratios along and on either side of the CIFALPS profile (Modified from Solarino et al. 2018).

Transformations of the crustal and mafic lithologies have been evidenced by geophysical imaging in several large scale orogens. Depth imaging show progressive transformation of the lower crust when imbricated in the orogenic wedges. In the central Andes, from receiver functions, the Moho and then the subducted oceanic crust are visible down to 120 km deep. Yuan et al., 2000 interpreted it as the effect of eclogitization. They thereby conclude that the gabbro-eclogite metamorphic reaction is kinetically delayed. According to thermodynamics, this reaction should have occurred at shallower depths. Similar observations lead some studies (Schulte-Pelkum et al., 2005 and Zhang et al., 2014) to claim the presence of intense shear zones at the lower crust scale. In the Himalayas, the dependance of the slab signature to the back azimuth of the computed seismic rays is interpreted as the consequence of 10 km-thick shear zones at the top of the Indian lithospheric crust (Nabelek et al., 2009 and Schulte-Pelkum et al., 2005). In the Alps, current studies (CIFALPS, CIFALPS2 and AlpArray, Fig.1) are showing geophysical images with a high enough resolution to highlight a possible impact of metamorphic reactions. We observe that the slab disappears around 70 km deep (Figure 1B). This phenomenon is commonly explained by the eclogitization of the lower crust or serpentinization of the overlying mantle, removing any contrast in velocity with the surrounding mantle.

Thus, rock transformation is carried out both by metamorphic reactions and by the fabric development on a large scale. These transformations have an impact on seismic velocities : they change both the bulk intrinsic properties of the rock, but also their anisotropy. As the above studies show, geophysical images not only make it possible to locate the major contrasts in the subduction/collision zones, but also to determine their petrological and structural significance. The first order metamorphic reaction able to have an impact are actually few : partial melting, that produce a low velocity fluid (Shapiro 2004, Hacker, 2014) or eclogitization, that crystallize high velocity phases such as garnet. At the mineral scale, only few minerals have a distinctive signature : amphiboles and phyllosilicates for instance yields high anisotropy (Schulte-Pelkum et al., 2015, Hacker, 2014). Limits of their stability fields are therefore expected to be seen in the geophysics. In this project, we focus on mafic lithologies, for which the amphibolite to eclogite transition is likely to alter both anisotropy (due to the consumption of amphiboles) and bulk seismic velocity (thanks to the crystallization of garnets). All the question is to know whether these changes are quantitatively large enough to be seen in the geophysics. We will also focus on their signature in the Vp signal (bulk and tensor values) since most of the relevant images of the Alpine slab are derived from P-wave analysis so far.

B. Eclogitization from a petrophysical perspective

To allow a quantitative approach to the effect of eclogitization in these images, it is essential to understand how this process modifies the seismic properties of the rocks. Studying the internal structure of the plunging crust therefore requires reasoning with fossil subduction and collision zones outcrop. Since these have been buried and then exhumed, they carry valuable information about the active processes at depth.

Experimental and field studies show how rock transformation has an impact on large-scale seismic properties (e.g. Zertani, 2020). Numerous studies attest that modal proportions but also crystal preferred orientations (CPO) and the distribution of minerals in rocks control the propagation of P- and S-waves (e.g. Bascou et al., 2001, Faccenda et al., 2019, Kern et al., 1997). Hence seismic properties of rocks are controlled by their chemical composition plus the degree they equilibrated along their PT path, plus their strain history. The fluid budget has also an impact on all these aspects of rock transformation into eclogite, via control of reaction kinetics, incorporation in phases (such as phengite for instance) or activation of specific strain mechanism (fluid assisted GBM for instance).

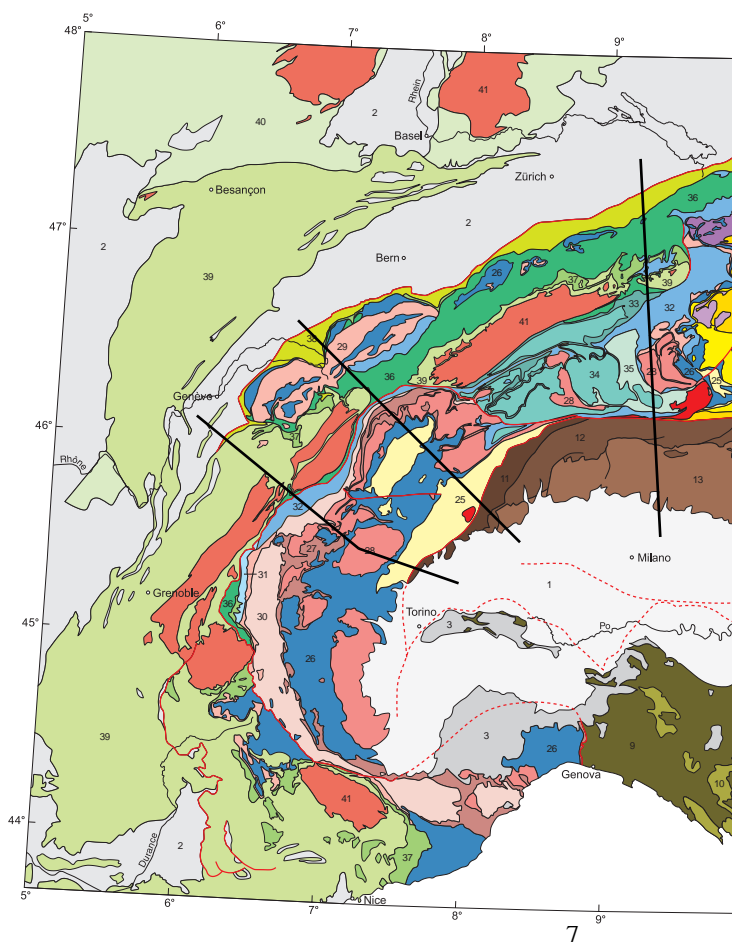
Moreover, recent studies on the Caledonides of Norway (Zertani 2020) show that the eclogitic/granulite ratio impacts the effective properties of the environment much more than the geometry of

the eclogitic shear zones. They also indicate that both inherited and newly formed anisotropies can be seen, mainly through back-azimuth, and that these can reach 5% on the kilometric scale.

C. The alpine slab : geological context and geophysical signature

The Alpine chain is part of a much larger orogenic belt, involving the entire surrounding area of the current Mediterranean and extending to the Himalaya (Piromallo & Faccenna, 2004). This short segment was formed as a result of subduction of the Thethyan-Ligurian Ocean under the Apulia Plate from the Upper Cretaceous to the Lower Eocene. Then, in the Middle Eocene, the continental margin involved in subduction, as attested by the presence of felsic UHP rocks from the Dora Maira massif (Chopin, 1987, Schmid et al., 2004, Figure 2). This chain is traditionally split into 2 main domains; on the one hand the external domain, which correspond to the units only involved in the collision (i.e., ECMs, Subalpine chains), and on the other hand the internal units, involved in subduction and then in the collision.

In 2015, Zhao et al., reveal for the first time, from seismic images, that the dipping slab, at a depth of 75 km, is connected to the European crust (Figure 1B). They also show that wave conversion on the European Moho has a lower amplitude in observations than in synthetics. They interpret this as the effect of the eclogitization of the lower crust, at depths greater than 40 km, under the penninic thrust, where the reflective lower crust (and Moho reflection) disappears. That being said, geophysical signals do not suddenly disappear but decrease as the lower crust transforms into eclogite. Recent studies clarified the structure of the inner prism (Malusa et al., 2017, Solarino et al., 2018) in particular the Ivrea body geometry but are not sufficient to conclude on the nature of the dipping slab and the units sitting on top of the crustal sliver. Serpentinized mantle, ultra high pressure (UHP) metamorphic slivers, are the currently debated alternatives. The CIFALPS profiles also highlight some unexplained features of the diving plate. At around 30 to 40 km depth, while the P/T field is supposed to be cylindrical, the increase in V_p is not (Solarino et al., 2018, Figure 1C).



Besides, some slow velocity and V_p/V_s domains locally occur at depths, where uniform velocities are expected (zone c in Figure 1C).

The present internship, aims at departing from rocks to investigate what specificities could explain these oddities in the geophysical signal.

II. State of the art

A. Advances in geophysics

As early as the 1980s, large geophysical profiles (ECORS, CROP, NFP-20, Figure 2) were carried out across the Alps in order to identify the nature and structure of the Alpine crust.

This approach is based on a reverse method: from seismic velocities, they deduce the petrophysical properties of the rocks at depth and mainly at the interfaces which generate high seismic contrasts. These calculations concerned especially the one of V_p from densities at surface conditions.

The ECORS profile first allowed to highlight the structure of the European crust (Fig.1A). It is double-layered with a densely layered lower layer at least beneath the ECM. Unfortunately the ECORS profile is blind under the inner wedge. Then, thanks to FR images, very sensitive to contrasts, we had evidence of a continuous slab with evolving properties and contrasts toward its surrounding units. (Fig.1B, Zhao et al., 2015). This slab itself has a signature that depends on the orientation of the seismic rays used for the FR analysis. With rays from the East (Fig.3B), its image is more continuous, while it is shorter and more discontinuous when imaged from the N (Fig. 3C). This means that contrasts are sharper when seen from the east, probably due to a significant internal anisotropy.

B. Progress on the seismic properties of the rocks

On the petrological data side, seismic anisotropy results from a combination of mineral anisotropy (rock fabric) and petrological heterogeneity (foliation). A complementary way to the geophysical method, to obtain the seismic properties of rocks is to calculate them from samples, i.e. by a direct method. Still, there is a lack of knowledge concerning the seismic properties of the rocks that make up the continental crust.

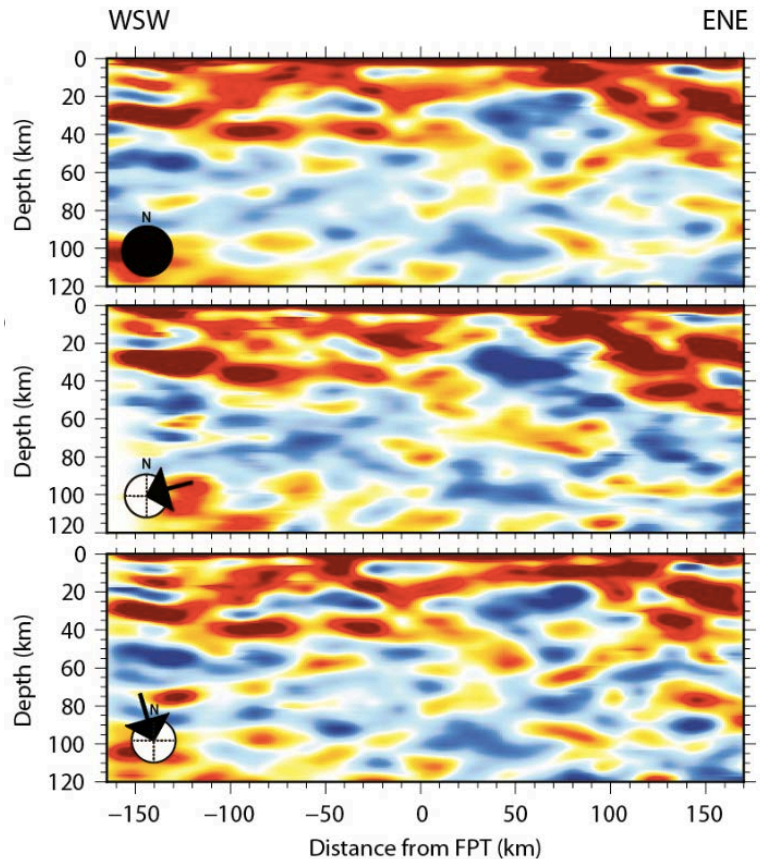
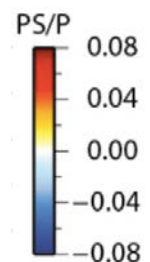


Figure 3: CCP depth sections computed for events with different ranges of back- azimuth.

- A. All back-azimuths.
- B. ENE back-azimuths.
- C. NNW back-azimuths.

The amplitude scale is the same for the 3 sections. From Zhao et al. 2015, supp-mat.



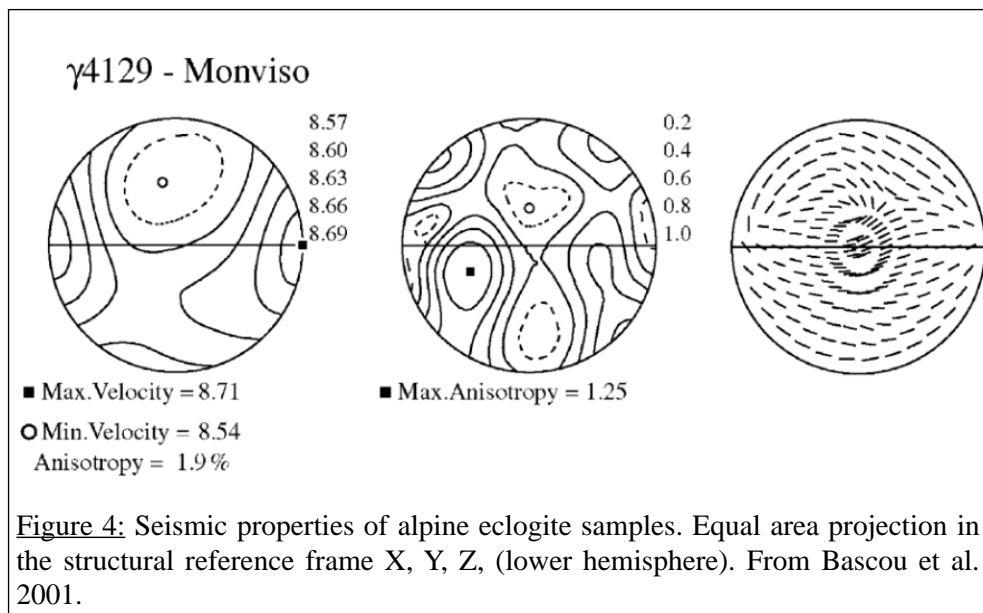
There are only measured values at sporadic PT conditions, some modeled, others calculated. Some consider pressure, temperature or fabric effects, others do not.

Among the existing studies, that of Barruol and Mainprice 1993 focuses on the Ivrea zone, representative of the lower alpine crust from the upper plate, while that of Bascou et al., 2001, for example (fig.4), gives values for eclogites from the Monviso and Sesia zones. It shows, among other things, that despite their very low anisotropy (less than 3% for the P and S waves), eclogites have maximum P-wave velocities parallel to linearization and by a minimum velocity normal to foliation. Based on its high seismic velocities ($V_p \sim 8.6$ and $V_s \sim 4.9$ km/s) and reflection coefficients, it indicates that the eclogite/crust interface is a good reflector, whereas an eclogite in the upper mantle would be difficult to see.

However, it is possible to calculate seismic properties (V_p , V_s and anisotropy) for an aggregate with known proportions and fabric (Lloyd et al 2011; Almquist & Mainprice 2017) and make corrections for the effect of grain boundaries or micro-cracks at varying pressures and temperatures (Motra & Zertani, 2018).

C. The help of numerical models : bring the gap in the scale transfer

Experimental measures of seismic waves velocities are performed in apparatus with high frequency signal, while seismic waves in nature are low to very low frequency. Hence the scale transfer must be validated via numerical modeling (e.g. Zhong et al., 2014) to predict the response of aggregates to wave propagation for variable frequencies. Thus, thanks to the numerical techniques deployed, a catalogue of synthetic seismic signatures of the rocks of the continental crust is fully accessible through different methods. In 2000, Frederiksen and Bostock, developed a method for the production of synthetic FRs. This allows the prediction of the impact of a given contrast geometry (Schneider et al., 2013) on a given wave path. In addition, the equivalent anisotropy at upper scale of a complex structure at lower scale can be found using the elastic tensor calculation method (Zertani, 2020). Finally, Fourier transform homogenization, which simplifies partial differential equations and encompasses several scales (Capdeville et al., 2015), provides access to the anisotropy image of a given structure (Alder et al., 2017).



This allows us to conclude that there has been a great methodological advance in geophysical methods (resolution and interpretation) but also in numerical tools and modeling on the seismic properties of rocks.

Since tomographic images are affected by rocks properties, today, we are able to evaluate the seismic anisotropy of samples with precision, thanks to a better knowledge of the properties of

minerals and aggregates. This accuracy makes it possible to discern rocks such as eclogite and peridotite, for which seismic anisotropy would be the discriminating parameter (Bascou et al., 2001 and 2011). For example, figure 4 shows us the seismic properties of an eclogite calculated from EBSD analyses.

Thus, this seismic resolution is fundamental in the 3D understanding of the Alpine structure, which is justified by the 3D nature of the anisotropy and that the Alps are not cylindrical. What remains to be done is to build a stronger link between these two fields and make them mutually reinforcing. This internship is part of this objective, without claiming to establish a complete link, it aims to show the feasibility of the approach.

III. Approach and results

Since the Alpine collision wedge is almost exclusively formed of upper crust (Figure 2), it is highly probable that the corresponding lower crust has been subducted into the mantle and is therefore responsible for the strong visible wave conversions along the slab (e.g. Zhao et al., 2015, Figure 1&2). A way to elaborate on this hypothesis is to find remnants of this lower crust in the field, measure their petrophysical properties and calculate the possible evolution of these properties

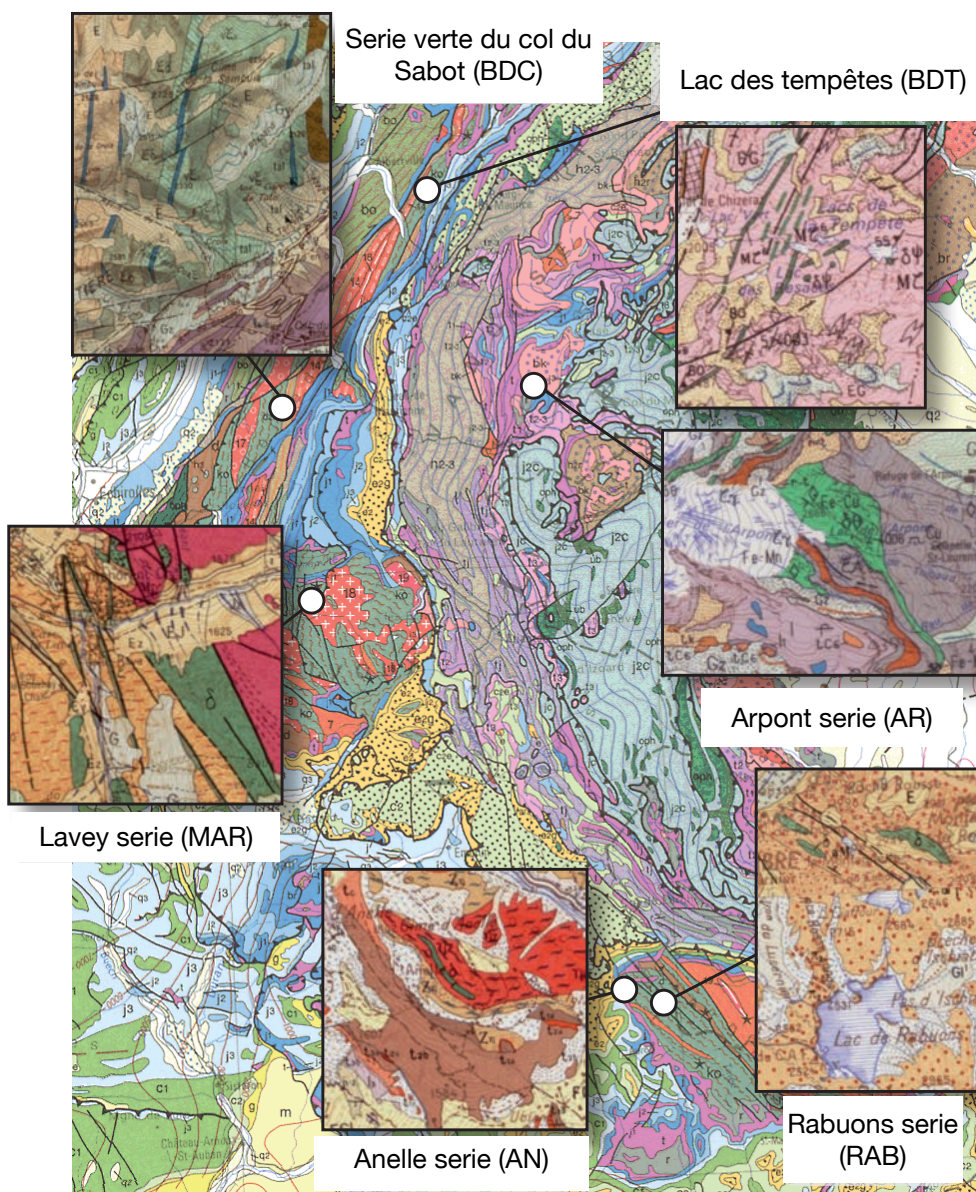


Figure 5: Sampling spots map. Modified from BRGM maps.

during burial. This, might even explain the variations in properties observed at the top and base of the dipping panel, through eclogitization or strain localization.

Since the slab seems to be characterized by a slight anisotropy (Zhao et al., 2015), we need to calculate and/or model the isotropic and anisotropic seismic velocities of the rocks. Among the lithologies likely to reflect the petrophysical properties of this lower crust, we focus on mafic lithologies, less subject to metamorphic reactions during burial, since they were metamorphosed during the Hercynian orogenic cycle. Thus, in this case, the most anisotropic minerals are amphiboles.

Therefore, this approach is based on two assumptions: the alpine lower crust forms the top of the subducting lithospheric panel and the intermediate to mafic rocks of the external crystalline massifs (ECM) are analogue to the subducting lower crust. The strategy of this project is twinned.

On the one hand, it consists in modeling the possible evolution of seismic properties during their burial, via bulk rock chemistry (ICP-OES analyses), pseudo-section and PT path models, yielding the evolution of isotropic component of the velocity tensor; on the other hand, in calculating the seismic properties of rocks, at surface conditions, thanks to Lattice Preferred Orientation (via EBSD) studies, providing access to the full anisotropic velocity tensor.

During their burial, 3 scenarios are involved: either the crust is not modified, in which case the surface samples are straight representative of those at depth, or the continental plate has completely reacted, and thermodynamics can give us the expected paragenesis and properties, or the signature of the slab is dominated by strain and therefore LPO from mylonites are the best analogues. It is obvious that there is a wide range of possible combinations between these 3 theoretical poles and it is only through real data that we will be able to identify the contribution of each scenario.

Location	Sample	GPS point	Type of rocks
Argentera massif - Annelle serie	AN1901, AN102, AN1903	44°15.426 - 006°55.269 - WP 120	amphibolite
	AN1904, AN1905, AN1906	44°11.314 - 007°02.525 - WP 111	
	AN1907, AN1908	44°10.843 - 007°03.06	
Argentera massif - Rabuons serie	RAB1901 (AetB), RAB1902	44°10.847 - 007°03.380 - WP 113	eclogite, amp
	RAB1903, RAB1904, RAB1905	44°28.4448 - 006°97.9911 - 2809m	amphibolite
	RAB1906, RAB1907	44°26.9393 - 006°97.8429 - 2498m	amp, gneiss
Arpont serie	AR1901	45°31.887 - 006°77.969 - 2622m	gneiss
	AR1902	45°31.892 - 006°77.800 - 2624m	amphibolite
	AR1903, AR1904	45°31.7586 - 006°77.7253 - 2692m	
Belledonne massif - Lacs de la tempête	BDT01	45°62.2109 - 006°54.7418 - 2132m	gneiss
	BDT02	45°62.1514 - 006°53.6120 - 2079m	amphibolite
	BDT03	45°62.1328 - 006°52.9289 - 2105m	
	BDT04, BDT05	45°62.1113 - 006°53.3851 - 2111m	
	BDT06	45°62.1338 - 006°52.9300 - 2061m	
	BDT07	45°62.2609 - 006°53.1439 - 2107m	
	BDT08	45°63.1502 - 006°54.3435 - 2568m	granite
Belledonne massif - Lac de Sainte Croix	BDC01	45°25.5398 - 006.14.6047 - 2328m	gneiss
	BDC02	45°25.5176 - 006°14.5820 - 2246m	amphibolite
	BDC03	45°25.5129 - 006°14.5731 - 2200m	
	BDC04	45°25.7452 - 006°14.6001 - 2434m	
	BDC05 (BDC05)	45°25.7421 - 006°15.0955 - 2392m	serpentinite
	BDC06	45°25.7401 - 006°15.0885 - 2372m	
Gassaudia	GAS01	44°93.4827 - 006°19.0551 - 1548 m	mica schist
	GAS02	44°93.6097 - 006°19.0993 - 1557 m	
Mariande	MAR1901, MAR1902, MAR1903	44°91.9572 - 006°16.9915 - 2083 m	gneiss

Table 1: Synthesis of the sample locations and nature of the rock

A. Sampling

The study area targets mafic to intermediate lithologies exposed in alpine crystalline units (intercalations within the ECMs) that are likely to represent lower crust lithologies. These are reasonably less subject to significant changes in their chemistry (e. g. by partial melting) during burial, since they represent restitic or refractory lithologies.

Thus, on July, August and October 2019 I sampled the mafic and intermediate rocks previously targeted mostly in the ECMs. In figure 5 are located the 6 sampled series.

Location	Sample	Foliation / Lineation	Microscope observations			Type of rock	Relevance	ICP-OES analysis	EBSD analysis
			Minerals	Deformation	Grain size				
Argentera massif - Annelle serie	AN1901	-	amp, pl qz	-	very coarse	amphibolite	-	-	-
	AN1902	no lineation	amp, qz, fsp	-	-		A	yes	-
	AN1903	-	amp, qz, fsp	-	-		-	-	-
	AN1907	both	amp, qz, fsp, ms, bt	stretching	> 1mm to 30 μm		A	yes	yes
Argentera massif - Rabuons	RAB1901A	both	grt, hbl qz, omp	symplectite (amp, qz, or)	2,5mm to 100μm	eclogite	A	yes	yes
	RAB1902	rare lineation	amp, grt, pl, qz, sil	-	3,4mm to 40μm	grt bearing amphibolite	A	yes	-
	RAB1903	-	amp, ms, pl, ep	-	500 to 200μm	amphibolite	B	-	-
	RAB1904	both	amp, ms(-), pl, ep, cpx	-	2mm to 60μm		A+	yes	yes
	RAB1905	-	amp, pl, spn	-	3,7mm to 50μm	B	-	-	
	RAB1906	rare lineation	amp, pl qz, altered grt	-	4mm to 30μm	grt bearing amphibolite	A-	yes	-
	RAB1907	both	bt, ms, pl, qz	CS shear	3mm to 70μm	bt bearing gneiss	A	yes	-
Arpont	AR1901	-	chl, qz, ms	-	-	chl bearing gneiss	C	-	-
	AR1902	-	chl, qz, ms, grt, inclusions	shear	-	amphibolite	-	-	-
	AR1903	rare lineation	amp, helicitic grt, pl, qz, ep, cb	shear	-	grt bearing amphibolite	A	yes	-
	AR1904	no lineation	ep, grt, amp, qz, oxides	shear and PS	-		A+	yes	-
Gassaudia	GAS01	-	qz, chl, ms	high shear	fine	mica schist	-	-	-
	GAS02	-	qz, chl, ms	high shear	fine		-	-	-
Mariande	MAR1901	rare lineation	qz, ms, chl, pl	CS shear, PS	fine	gneiss	A	yes	-
Mariande	MAR1902	-		CS shear	-		C	-	-
	MAR1903	rare lineation			-	amphibolite	A	yes	-
Belledonne massif - Lacs de la tempête	BDT01	both	qz, amp, ms, oxides, speckled matrix	shear and qz band	-	gneiss	A	yes	-
	BDT02	-	bt, ph, chl, amp, pl, qz	high shear	1,5mm to 1μm	amphibolite	B	-	-
	BDT03	rare lineation	g hb, qz, pl and matrix	pseudoM de grt et OP	1,4mm to 1μm		A	yes	-
	BDT04	-	pl, qz, bt, grt, ms, ep, amp	-	-	gt bearing amp, GS facies	C	-	-
	BDT05	rare foliation	grt, hb, pl, ms, qz	-	5mm to 50μm		A	yes	-
	BDT06	-	altered grt, hb, pl, ms, qz	symplectite (ms and qz)	5mm to 100μm	gt bearing amphibolite	C	-	-
	BDT07	both	90% oriented and stretched amp, ru, qz, cpx, ms	-	5mm to 10μm	amphibolite	A	yes	-
	BDT08	-	pl, qz, bt and chl or amp	-	-	granite	D	-	-
Belledonne massif - Lac de Sainte Croix	BDC01	-	chl, bt, qz, pl	-	2mm to >3μm	gneiss	D	-	-
	BDC02	-	amp, fsp, qz, chl, ep	high shear	3mm to 5μm	GS facies amphibolite	A	yes	-
	BDC03	rare lineation	g hb, oxides, qz, pl, ep	CS shear	700 to 80μm	amphibolite	A +	yes	-
	BDC04	both	g hb, oxides, qz, pl, ms	-	900 to 200μm	amphibolite	A	yes	yes
	BDC05	-	opx altered to serp., qz, chl	-	500 to 50μm	serpentinite	D	-	-
	BDC06	-	serpentine, qz, opx, chl	-	500 to 50μm	serpentinite	D	-	-

Table 2: Synthesis of microscopic observations for each sample. Abbreviations are from Whitney and Evans, 2010. In bold are the samples on which the EBSD measurements were made.

The two first ones are located in Belledonne Massif : one at the Lacs des Tempêtes (BDT samples) and the other Série Verte from Col du Sabot, near the Lac de Saint Croix (BDC samples). Others were sampled in the Oisans massif, as mafic intercalations in the Lavey migmatites (MAR) and the Rabuons and Annelle series, in Argentera massif (RAB and AN samples).

The MCEs represent old tilted blocks of the European margin and are part of the Dauphinois basement, which corresponds to the middle Hercynian crust, now exhumed (Gap or Annecy geology map, 1/250 000, BGRM). Finally, the Arpont series was sampled in the Vanoise massif (AR samples), which corresponds, this time, to the Briançonnais basement and represents an old proximal tilted block, cut out during the Jurassic and then strongly deformed.

The majority of the samples are amphibolites with traces of greenschist facies retrogression for some of them. The rest correspond to some gneisses typical of the surrounding rock and a relatively fresh eclogite.

Table 2 summarizes microscopic observations for each sample, classified according to sampling spots. The « relevance » column notes the suitability of the thin section as a lithological analogue of the lower crust.

Figure 6 is an example of a polarized light microscopic picture of thin section.

Sample in figure 6 (RAB1904) comes from Rabuons serie and is interpreted as an amphibolite, since we observe the following paragenesis: green hornblende, epidote, plagioclase and quartz. In this sample, foliation and lineation were easily recognizable, although there are a few misoriented amphiboles (ie with the basal section (120° cleavages) in the XZ thin section plane), and the finite strain reference frame is well set. From the same serie, sample RAB1901A is a well preserved eclogite rich in garnets, surrounded by amphiboles, with some quartz, omphacite and rutiles.

Similar to RAB1904, sample BDC04 contains a lot of amphiboles and plagioclases and some quartz. Yet, its amphiboles have a quite different fabric, they do not seem oriented, while those of RAB1904 are. Lastly, AN1907, from Annelle serie, is composed of micas (biotite and muscovite), amphiboles and quartz and shows a fabric mainly carried by biotites.

B. Methods

1. Bulk rock chemistry

To know the chemical composition of major elements on bulk rock samples, I performed ICP-OES (Inductively Coupled Plasma with Optical Emission Spectrometer) measurements. Samples are dissolved in a combination of acid and excited by argon ions in the plasma. When returning to more stable excitation levels, the excited electrons release photons. The OES then measures the intensity of the radiation emitted at the characteristic wavelengths of the elements. By converting the intensities into elemental concentrations using standards, it is possible to determine the elements present and their concentrations.

However, emission patterns can be complex and spectral interference is possible if the wavelengths of the elements under consideration overlap. For this reason, obtaining the trace element compositions from this instrument is not straightforward.

In this study, I analyzed the major element composition of 18 samples, each measured twice, in order to get a duplicate analysis. Two dilutions were also performed (one at 1000 and the other at 10 000) that one may avoid spectral interference phenomena by supersaturated elements. When the duplicate values fall in the uncertainty domain of the instrument, their average has been taken as a result.

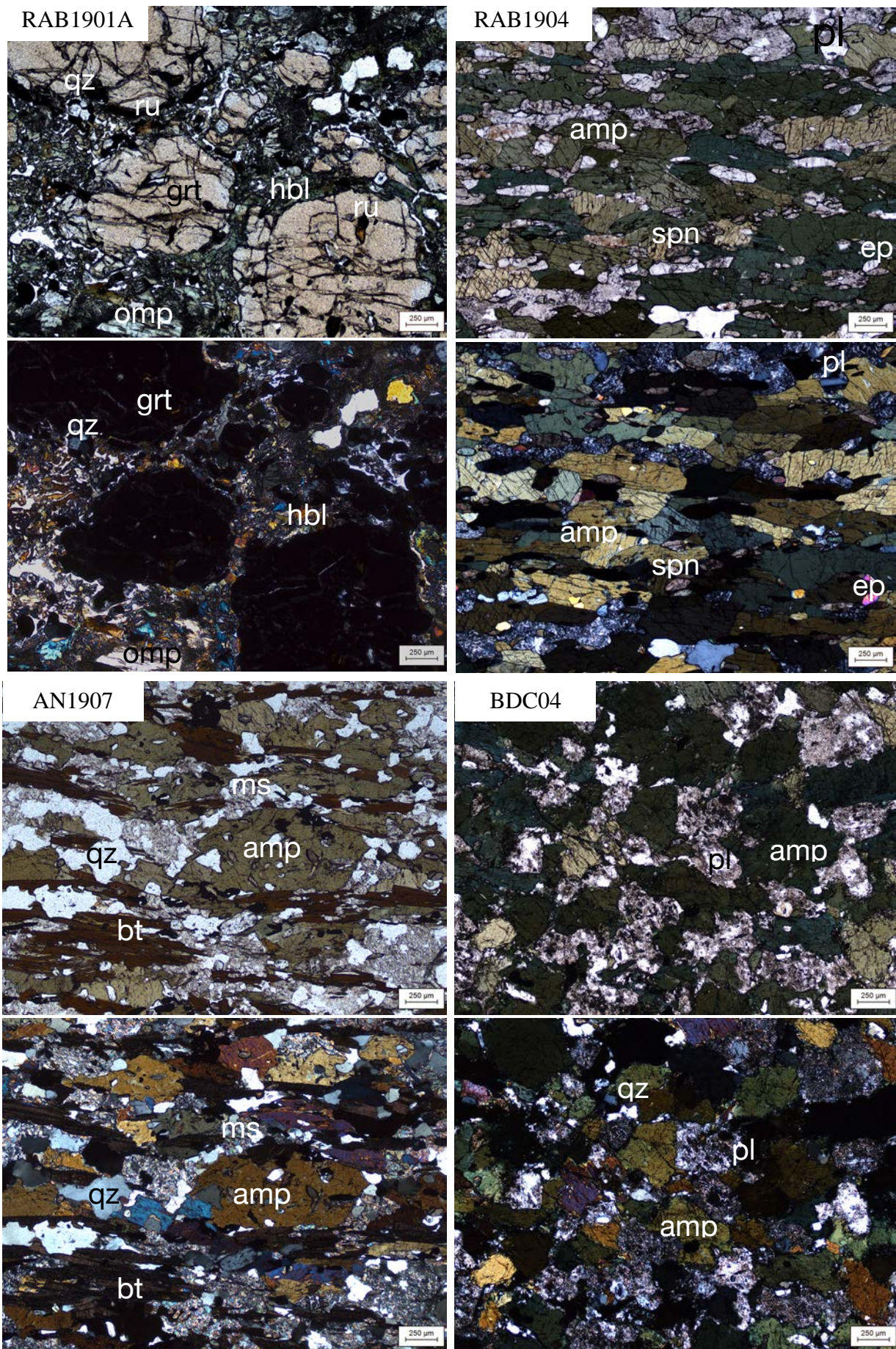


Figure 6: Microscopic photo of thin sections of 4 samples on which the EBSD analyses were performed. This thin section were been made perpendicular to the foliation and parallel to the lineation.

2. Thermodynamic and seismic properties modeling

The thermodynamic evolution of the parageneses during burial was performed using the TheriakDomino program (Capitani and Petrakakis, 2010). Nine increasingly complex chemical systems have been tested : NCF(and/or M)AS, (K)NCF(and/or M)ASH, with stoichiometric amount of H and excess H₂O. NCFMASH seems to be the most adequate system since it represents all the phases present and in the correct quantity, and has been used to compute modal proportions on a regular PT grid.

Nevertheless topology of the PT space has been deciphered in NC(F+M)ASH with all Fe and Mg considered as Fe, to avoid complex divariant reactions.

Modal proportion PT grids were processed using a MATLAB code and then used to deduce the evolution of the seismic properties of the rocks during their burial thanks to the Matlab script of Abers & Hacker 2016, that allows to estimate bulk V_p and V_s for given paragenesis and PT conditions. This script uses intrinsic mechanical and thermic properties, such as alpha, the thermal expansion coefficient, K the incompressibility modulus and G, the shear modulus, for each mineral phases and their partial derivatives along P and T to compute average V_p and V_s from modal proportions and PT conditions. At the end, the seismic velocity of the bulk rock is deduced from the seismic velocities of each mineral phase. By default, we used the Hill average since the Reuss and Voigt averages favour end-member scenarios.

3. Lattice Preferred Orientations

In order to determine the crystallographic orientation of the minerals, which is a factor influencing the non isotropic part of seismic properties of the rocks, EBSD (Electron Backscattered Diffraction) analyses were carried out. It allows to obtain the different crystallographic orientations of the grains in a sample and to identify the phases present. To do this, an electron beam, generated by a scanning electron microscope (SEM) obliquely strikes the surface of the sample. The interaction with the crystallographic planes of the sample deflects the electrons and generates diffraction cones (Fig.7), the angle of which follows the Bragg's law:

$$n\lambda = 2d\sin\theta$$

where n is the order of diffraction, λ the wavelength of the electrons, d the inter-reticular distance and θ the angle of incidence of the electrons.

During the analysis, the sample is tilted at 70° so that the emission of the backscattered electrons is maximal. In the EBSD detector, these cones are detected by a CCD sensor placed behind a phosphor screen. The intersection between this screen and the cones form lines that intercept each other and are called Kikuchi bands. EBSD analysis is based on the study of these bands: their number, arrangement, intensity and width are characteristic of the crystal lattice of a mineral. Thus, for each identified phase, it is possible to study its fabric, ie the orientation of its crystallographic axes in the thin section reference frame (Euler angles). Sometimes, the crystallographic indices of certain phases are too close to allow their distinction. In this case, a combined EDS (Energy

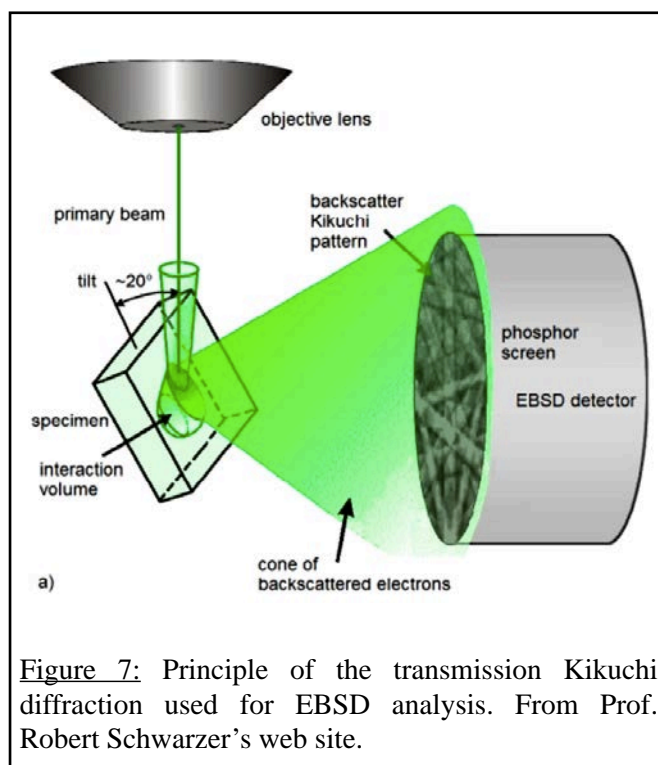


Figure 7: Principle of the transmission Kikuchi diffraction used for EBSD analysis. From Prof. Robert Schwarzer's web site.

Dispersive X-ray Spectroscopy) analysis is beneficial. This detects the X-rays emitted by the excited surface of the sample when it is bombarded with an electron beam. The energy spectrum of the emitted X-rays is unique to each element and allows the elemental composition of the sample volume to be determined.

In this study, 4 samples of eclogitic and amphibolite facies (RAB1901A, RAB1904, BDC04 and AN1907), taken from mafic and intermediate group were analysed. They were previously classified according to their chemical composition thanks to ICP analysis and selected by their relevance and in such a way that they are representative of all samples. Crystallographic orientation measurements were made using a scanning electron microscope (SEM), from Ecce Terra platform, and combined with an EDS analysis. The thin, polished sections were made parallel to the lineation and perpendicular to the foliation (ie in the XZ plane). The measurements were done by O. Boudouma during the confining period, and the processing of the data performed as soon as I could come back in the lab.

The resulting maps were processed using MTEX, a MATLAB toolbox. The stitching of EBSD snapshot into larger bands was necessary due to the large grain size of my samples. The distortion of the sensor had to be corrected to properly reconstruct grains. To define a whole grain, threshold misorientation angle (difference in Euler angles between two adjacent pixels) has been set to 10° , while sub-grains are defined by misorientation angles between 6 and 10° . Hence, the sampling step directly influences the amount of grain detected since a small sampling step will detect more grains but also reveal continuous disorientation where larger sampling step will yield a grain boundary. The crystallographic orientations are eventually shown in pole figures, represented in lower hemisphere projections in sample reference frame, where the lineation is represented by X, the foliation by the XY plane and the direction normal to the foliation by Z.

To compute seismic velocity tensors from Euler angles, it is necessary to provide the stiffness tensors of each mineral composing a sample, their crystalline symmetries, as well as their orientation (specified in the .ctf file). Average velocities can be directly calculated by averaging properties over all the pixels. My maps easily reach 2 millions pixels, therefore I calculated orientation density functions (ODF) for each phases, and then balance these with modal proportions. This allows faster calculation, and also allows to keep only major phases and possibly play with their proportions. Using ODF, stiffness tensors and modal proportions information, MTEX calculates the velocities, anisotropies and polarizations of seismic waves. Reuss, Voigt and Hill averages are systematically computed. Hill averages have been used in the present report.

C. Results

1. From bulk chemistry to PT velocity map

This section focuses on the effect of mineralogy on the seismic velocities of rocks. For this, in order to know the bulk composition of the samples, I performed ICP-OES analyses and then used these results in thermodynamic modeling to estimate the mineralogical evolution of the rock during its burial. From a database (Abers & Hacker, 2016), I deduced the associated seismic properties.

a) Major element composition of bulk-rock samples

Following microscopic and macroscopic observations, I selected the relevant samples (18, Tab. 2) and analyzed their bulk composition, thanks to ICP-OES, distributed as follows: 5 samples from the Rabuons series, 2 from each Lavey, Arpont and Annelle series, 4 from the Lacs de la Tempête and 3 from the Série verte du col du Sabot. 14 rocks out of 18 are amphiboles, 1 is eclogite and 3 are gneisses.

Table 3 summarizes the results of the analyses in percent by weight in oxydes. A distinction has been made between Fe_2O_3 and FeO, but I use $\text{FeO} + \text{Fe}_2\text{O}_3$ to calculate FeO + MgO total.

Samples	Oxides (wt %)											Total
	SiO2	Al2O3	FeO	CaO	MgO	Na2O	K2O	TiO2	P2O5	MnO	Cr2O3	
AN1902	51,5	13,8	14,3	8,6	6,1	3,0	0,8	2,3	0,3	0,3	0,0	100,9
	49,7	13,5	14,5	8,3	5,9	2,9	0,8	2,4	0,3	0,3	0,0	98,5
	50,6 ± 1,2	13,7 ± 0,2	14,4 ± 0,2	8,5 ± 0,2	6,0 ± 0,2	2,9 ± 0,0	0,8 ± 0,0	2,3 ± 0,1	0,3 ± 0,0	0,3 ± 0,0	0,0 ± 0,0	99,7 ± 2,2
AN1907	53,1	14,6	12,4	5,3	5,2	0,6	3,7	3,1	0,4	0,3	0,0	98,5
	52,8	15,0	12,9	5,2	5,2	0,5	3,7	3,2	0,3	0,3	0,0	99,2
	52,9 ± 0,2	14,8 ± 0,3	12,6 ± 0,4	5,3 ± 0,0	5,2 ± 0,0	0,6 ± 0,0	3,7 ± 0,0	3,2 ± 0,1	0,4 ± 0,0	0,3 ± 0,0	0,0 ± 0,0	98,8 ± 1,1
AR1903A	42,0	13,5	11,6	13,7	6,0	3,3	0,7	2,5	0,5	0,2 ±	0,0	94,0
	42,1	13,8	12,5	13,8	6,1	3,3	0,7	2,8	0,4	0,2 ±	0,0	95,5
	42,0 ± 0,1	13,7 ± 0,2	12,0 ± 0,6	13,7 ± 0,0	6,0 ± 0,0	3,3 ± 0,0	0,7 ± 0,0	2,7 ± 0,2	0,4 ± 0,0	0,2 ± 0,0	0,0 ± 0,0	94,7 ± 1,2
AR1904	49,7	14,9	14,4	7,9	4,8	2,8	0,5	2,5	0,3	0,2	0,0	98,0
	50,4	15,1	15,5	8,0	4,8	2,8	0,6	2,7	0,3	0,3	0,0	100,3
	50,1 ± 0,5	15,0 ± 0,1	14,9 ± 0,8	7,9 ± 0,1	4,8 ± 0,0	2,8 ± 0,0	0,5 ± 0,0	2,6 ± 0,2	0,3 ± 0,0	0,3 ± 0,0	0,0 ± 0,0	99,1 ± 1,7
BDC02	58,9	16,6	4,8	5,2	5,4	4,7	1,1	0,6	1,2	0,1	0,0	98,7
	57,9	16,5	5,1	5,2	5,4	4,8	1,2	0,7	1,1	0,1	0,0	97,9
	58,4 ± 0,7	16,6 ± 0,1	4,9 ± 0,2	5,2 ± 0,1	5,4 ± 0,0	4,7 ± 0,1	1,2 ± 0,0	0,7 ± 0,0	1,1 ± 0,1	0,1 ± 0,0	0,0 ± 0,0	98,3 ± 1,3
BDC03	51,5	17,2	10,7	6,3	5,2	4,4	1,0	1,9	0,3	0,2	0,0	98,7
	52,7	17,9	11,3	6,6	5,4	4,6	1,1	2,1	0,2	0,2	0,0	102,1
	52,1 ± 0,9	17,6 ± 0,5	11,0 ± 0,4	6,4 ± 0,2	5,3 ± 0,1	4,5 ± 0,2	1,1 ± 0,0	2,0 ± 0,1	0,2 ± 0,0	0,2 ± 0,0	0,0 ± 0,0	100,4 ± 2,5
BDC04	49,1	14,3	13,2	8,9	5,9	2,9	1,0	2,2	0,3	0,2	0,0	98,0
	50,7	15,0	14,2	9,2	6,2	3,0	1,0	2,4	0,3	0,2	0,0	102,2
	49,9 ± 1,1	14,6 ± 0,5	13,7 ± 0,7	9,0 ± 0,2	6,1 ± 0,2	3,0 ± 0,1	1,0 ± 0,0	2,3 ± 0,2	0,3 ± 0,0	0,2 ± 0,0	0,0 ± 0,0	100,1 ± 3,0
BDT01	67,8	15,8	4,2	2,0	1,9	2,6	3,7	0,6	0,9	0,1	0,0	99,5
	68,2	15,7	4,3	2,1	1,9	2,6	3,6	0,7	0,8	0,1	0,0	99,8
	68,0 ± 0,2	15,8 ± 0,0	4,2 ± 0,1	2,0 ± 0,0	1,9 ± 0,0	2,6 ± 0,0	3,7 ± 0,0	0,6 ± 0,0	0,8 ± 0,1	0,1 ± 0,0	0,0 ± 0,0	99,7 ± 0,6
BDT03	45,6	16,1	11,8	10,5	7,5	1,9	2,8	1,2	0,1	0,2	0,0	97,7
	45,6	16,0	12,3	10,5	7,5	1,9	2,8	1,3	0,1	0,2	0,0	98,2
	45,6 ± 0,1	16,1 ± 0,0	12,0 ± 0,3	10,5 ± 0,0	7,5 ± 0,0	1,9 ± 0,0	2,8 ± 0,0	1,3 ± 0,0	0,1 ± 0,0	0,2 ± 0,0	0,0 ± 0,0	98,0 ± 0,6

Samples	Oxides (wt %)											Total
	SiO2	Al2O3	FeO	CaO	MgO	Na2O	K2O	TiO2	P2O5	MnO	Cr2O3	
BDT05	49,0	13,8	13,8	9,1	8,1	2,0	0,5	1,1	0,2	0,2	0,0	97,8
	49,8	14,2	14,5	9,3	8,3	2,1	0,5	1,2	0,1	0,2	0,0	100,4
	49,4 ± 0,5	14,0 ± 0,3	14,2 ± 0,5	9,2 ± 0,2	8,2 ± 0,1	2,1 ± 0,1	0,5 ± 0,0	1,2 ± 0,1	0,2 ± 0,0	0,2 ± 0,0	0,0 ± 0,0	99,1 ± 1,8
BDT07	50,8	5,9	10,4	11,8	15,7	0,5	0,4	0,5	0,2	0,2	0,1	96,4
	51,1	6,4	10,9	12,1	16,2	0,5	0,4	0,5	0,2	0,2	0,1	98,5
	50,9 ± 0,2	6,2 ± 0,3	10,6 ± 0,4	11,9 ± 0,3	16,0 ± 0,3	0,5 ± 0,0	0,4 ± 0,0	0,5 ± 0,0	0,2 ± 0,0	0,2 ± 0,0	0,1 ± 0,0	97,5 ± 1,6
MAR1901	64,4	14,6	6,2	0,3	3,1	1,3	3,9	0,7	0,1	0,1	0,0	94,8
	68,5	15,8	6,6	0,4	3,3	1,4	4,0	0,8	0,1	0,1	0,0	100,9
	66,4 ± 2,8	15,2 ± 0,9	6,4 ± 0,3	0,3 ± 0,0	3,2 ± 0,1	1,4 ± 0,1	4,0 ± 0,1	0,8 ± 0,1	0,1 ± 0,0	0,1 ± 0,0	0,0 ± 0,0	97,9 ± 4,4
MAR1903	51,2	14,9	12,8	8,1	5,9	2,1	2,4	2,4	0,4	0,2	0,0	100,5
	49,9	15,2	13,9	8,1	6,1	2,1	2,4	2,6	0,4	0,3	0,0	100,9
	50,5 ± 0,9	15,1 ± 0,2	13,3 ± 0,8	8,1 ± 0,0	6,0 ± 0,1	2,1 ± 0,0	2,4 ± 0,0	2,5 ± 0,1	0,4 ± 0,0	0,3 ± 0,0	0,0 ± 0,0	99,7 ± 2,2
RAB1901A	44,6	15,4	16,3	10,2	5,3	2,9	0,2	2,7	0,6	0,2	0,0	98,4
	44,8	15,9	17,7	10,7	5,7	3,0	0,3	3,0	0,5	0,2	0,0	101,8
	44,7 ± 0,1	15,7 ± 0,4	17,0 ± 1,0	10,4 ± 0,3	5,5 ± 0,3	3,0 ± 0,1	0,2 ± 0,0	2,9 ± 0,2	0,5 ± 0,0	0,2 ± 0,0	0,0 ± 0,0	99,7 ± 2,4
RAB1902	51,6	13,9	13,0	8,7	5,8	2,7	0,7	2,0	0,4	0,2	0,0	98,9
	52,4	14,2	13,7	8,9	6,0	2,7	0,7	2,1	0,4	0,2	0,0	101,2
	52,0 ± 0,6	14,0 ± 0,2	13,3 ± 0,5	8,8 ± 0,1	5,9 ± 0,1	2,7 ± 0,0	0,7 ± 0,0	2,0 ± 0,1	0,4 ± 0,0	0,2 ± 0,0	0,0 ± 0,0	99,7 ± 1,8
RAB1904	42,7	15,7	14,0	12,9	5,1	2,1	1,7	3,6	1,0	0,3	0,0	99,1
	42,9	15,8	15,0	13,0	5,1	2,2	1,7	3,9	0,9	0,4	0,0	100,8
	42,8 ± 0,1	15,7 ± 0,1	14,5 ± 0,7	12,9 ± 0,1	5,1 ± 0,0	2,2 ± 0,1	1,7 ± 0,0	3,8 ± 0,2	0,9 ± 0,1	0,3 ± 0,0	0,0 ± 0,0	99,7 ± 1,4
RAB1906	50,3	13,1	14,0	8,4	5,6	3,0	0,7	2,8	0,4	0,3	0,0	98,4
	50,8	13,2	15,0	8,5	5,7	2,9	0,8	3,0	0,3	0,3	0,0	100,5
	50,5 ± 0,4	13,2 ± 0,1	14,5 ± 0,7	8,4 ± 0,0	5,6 ± 0,1	2,9 ± 0,0	0,7 ± 0,0	2,9 ± 0,2	0,4 ± 0,0	0,3 ± 0,0	0,0 ± 0,0	99,7 ± 1,6
RAB1907	69,9	14,9	5,5	1,9	1,7	2,4	3,1	0,7	0,3	0,1	0,0	100,5
	70,3	14,9	5,9	1,8	1,7	2,4	3,1	0,8	0,2	0,1	0,0	101,2
	70,1 ± 0,3	14,9 ± 0,0	5,7 ± 0,3	1,8 ± 0,0	1,7 ± 0,0	2,4 ± 0,0	3,1 ± 0,0	0,8 ± 0,0	0,2 ± 0,0	0,1 ± 0,0	0,0 ± 0,0	99,7 ± 0,7

Table 3: Results of ICP-MS measurements on 18 samples. For each sample, the first two lines correspond to the measurements, the last one to the mean and the standard deviation.

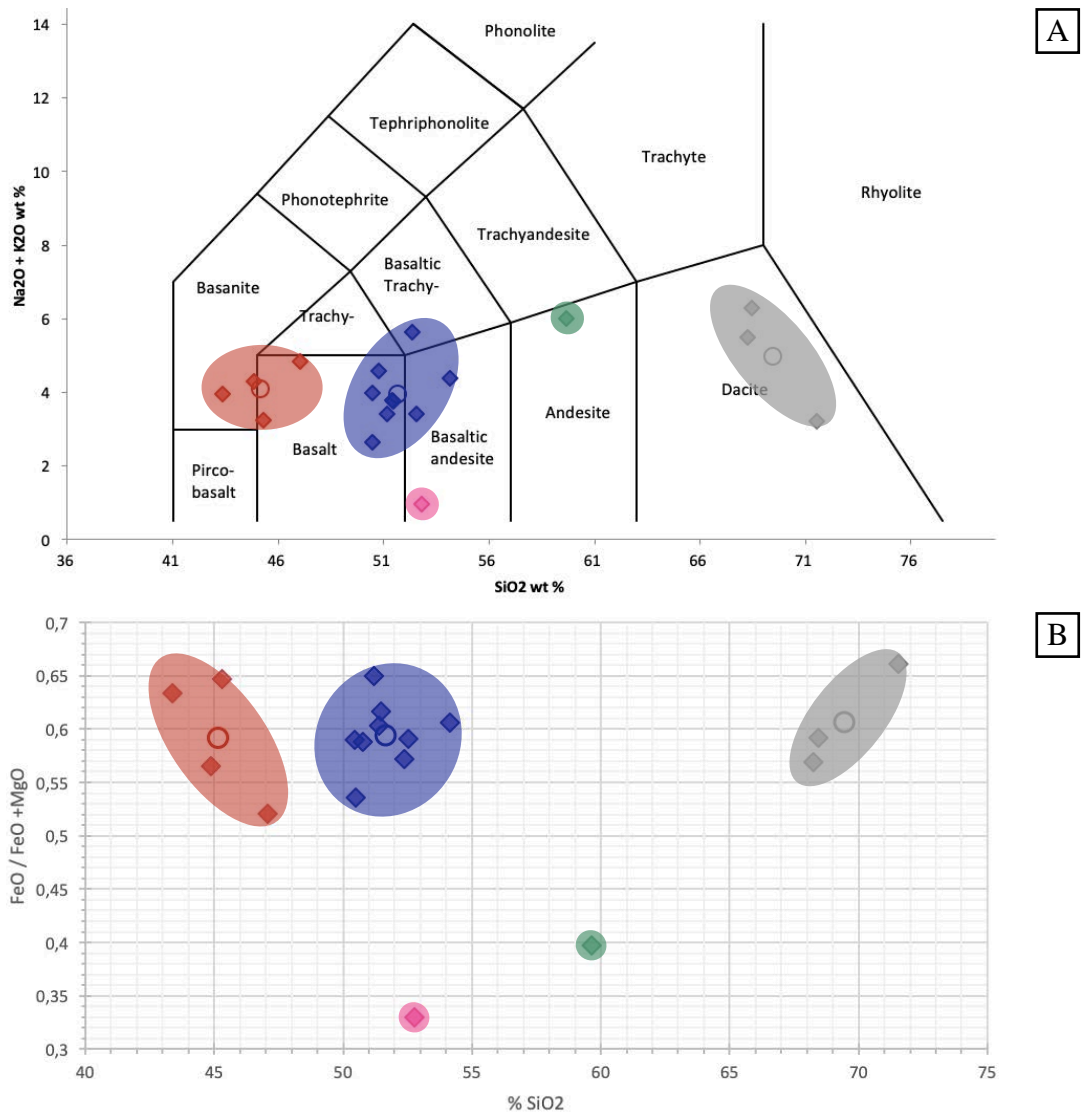


Figure 8: TAS diagram (A) and $\text{FeO}/(\text{FeO}+\text{MgO})$ Harker diagram (B). Samples are classified according to their Si and FeO tot contents. Mafic group under 50 % of Si, intermediate between 50 to 55% and gneiss around 70%. Felsic group is the green dot, i.e. BDC02.

Most of the time, the weights of oxides are quite the same for both dilutions. At worst, the standard deviation is less than 3%. In this way, weight measurements are reliable.

Then, in order to observe a possible correlation between samples, I have plotted the following diagrams (Fig.8): the Total Alkali Silica (TAS) and Hackers diagrams and the AFM (Al_2O_3 , FeO and MgO) and QAFP diagram. The colored dots in Table 3 indicate the chemical group to which the sample belongs.

TAS diagram compares the combined alkali content with that of silica. The sample distribution shows a spread along the x-axis, i.e. as a function of SiO_2 . Most of the samples are under-saturated in silica.

Harker graphs have been made for the following oxides: Al_2O_3 , $\text{FeO}/(\text{FeO}+\text{MgO})$, $\text{Na}_2\text{O} + \text{K}_2\text{O}$ (-CaO) and MnO (Fig. 8A). For more details on all graphs, see appendix 1.

The one comparing $\text{FeO}/(\text{FeO}+\text{MgO})$ display a similar distribution than TAS diagram.

Indeed, we get gneiss, shown in grey, around 70% SiO_2 . Then, nearly 60% silica, sample BDC02 is systematically isolated (shown in green). According to the thin section, this sample corresponds to

Pseudosection for the intermediate group is the simplest. It includes only a few minerals (garnet, omphacite, amphibole, feldspar, chlorite and olivine), while the one for the mafic group adds lawsonite and paragonite. In the latter, amphiboles are stable over a larger PT space than for mafic pseudosection and the first order reaction is the feldspar reaction: $jd + qz = ab$.

Pseudosection for felsic group, which corresponds to a highly retromorphic sample of the greenschist facies, is more complex as it involves much more minerals (garnet, amphibole, omphacite, feldspar, chlorite, kyanite and lawsonite). Hence, it includes eclogite bearing kyanite or eclogite bearing lawsonite and the garnet + omphacite stability field is reduced towards higher T and P.

Furthermore, from the same compositions and PT conditions, I built some gridded paragenesis diagrams. These diagrams store in each pixel of a PT grid, information on the mineralogical assemblages found (volumes, composition variations of a phase, etc) and save them in separate files.

c) Seismic properties modeling from mineral proportions

Abers & Hacker (2016) mineral properties database provides information for all the phases present in our thin sections. Thanks to this, we are able to estimate the seismic velocities of minerals and by using variations in phase volume, under PT conditions, we have access to the seismic velocities variations of rocks, in PT space.

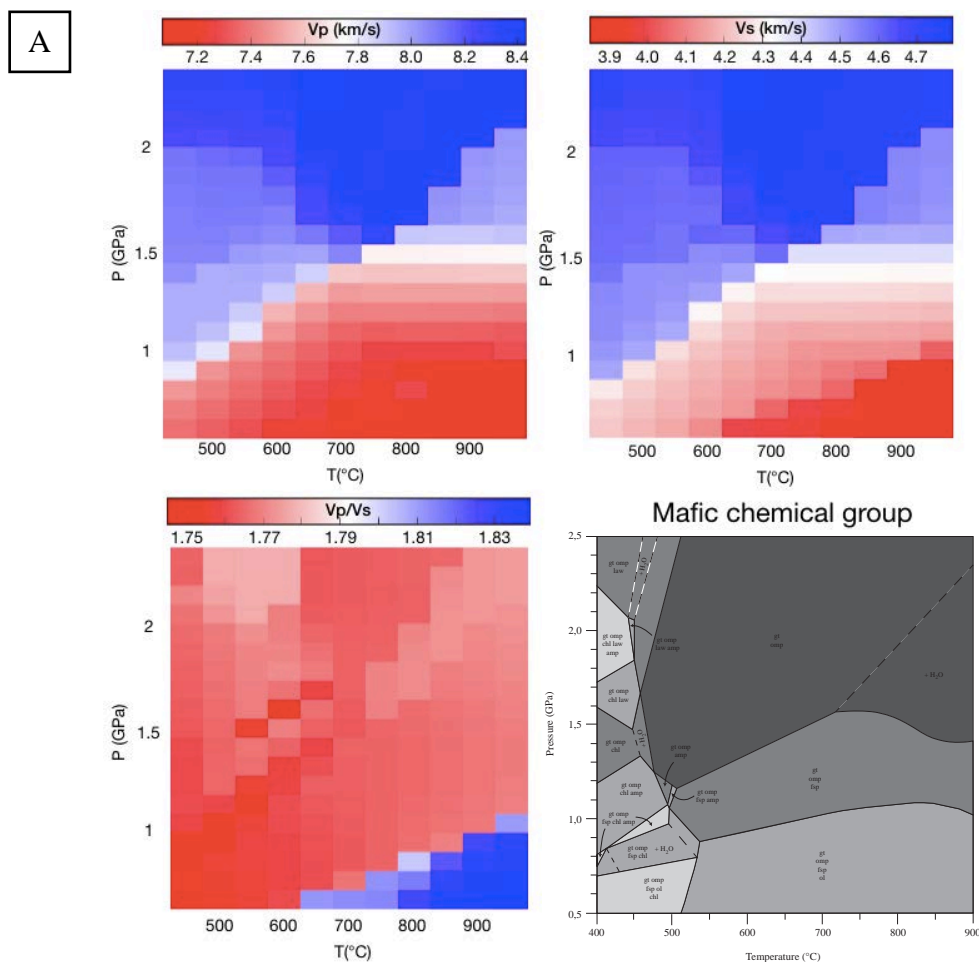


Figure 10: Results of seismic velocities modeling (V_p , V_s and V_p/V_s ratio) via Abers & Hacker, 2016 database, in PT space for a mean chemical composition for mafic (A), intermediate (B) and felsic (C) groups and the related pseudo-sections. Blue velocities are higher than red one, as in tomography.

Figure 10 shows the seismic velocity variations of P-wave (V_p), S-wave (V_s) and V_p/V_s ratio in a PT field for the 3 groups of different chemical compositions. The corresponding pseudo-section from Theriak-Domino is also reported for comparison. As in tomography, the seismic velocities are higher in blue than in red. Yet, the color scale differs according to the graphs.

For mafic group, the topology of V_p and V_s are similar, even if V_p/V_s ratio shows some differences, especially around the olivine stability field. This may be explained by a high olivine V_p range (Lloyd et al., 2011). Similarly, for the intermediate group, the P and S wave velocities show identical variations, which are also found in the V_p/V_s ratio.

While the V_s and V_p/V_s ratio for mafic and intermediate group are spread over a range of identical values, the V_p values are weaker for the intermediate group. In fact, the values of the mafic red field is that of the blue field for the intermediate and felsic groups.

For felsic, more constant seismic velocity fields are observed than for the previous groups, which is consistent with the more complex pseudosection. For instance, inside the blue velocity field, we identify 3 subfields, which correspond to the stability domains of the following 3 mineralogical assemblages: grt + omp, grt + omp + ky and grt + omp + ky + law.

Thus, the correspondence between pseudosections and seismic velocities in PT space shows that each constant velocity fields correspond to mineral stability fields. For each chemical group, high and low velocity fields are bounded by the reaction of the feldspars.

Only one constant velocity field does not match with chemical reactions. This field is an intermediate between those in red and blue, located just above the feldspar reaction. We interpret this as the result of the melting. Indeed, the parageneses used contain melt that has not been taken into account in the calculation of the velocities, due to its lack in the database.

Although it would be possible to add it, its seismic signature is highly dependent on its dispatch (connected vs. scattered droplets), which would require a lot of assumptions, at the risk of becoming less relevant.

In addition, the alpine slab has been locked in the lithospheric mantle since 30 Ma. This suggests that the melt from a possible partial melting stage is probably no longer in place. Thus, the weak blue field observed above the feldspar reaction is probably quite realistic.

2. From LPO to velocity tensors

A complementary approach to the previous one is, this time, to specify the seismic velocities taking into account the fabric of the rock.

To this end, I analyzed 4 thin sections via EBSD to obtain the orientation of the minerals within the sample and then by deducing the associated seismic velocities from the elasticity tensors of the rocks. This will give us access to the anisotropic part of the tensor, while the previous one allowed us to obtain information on the isotropic part, considering only the effect of mineralogical and chemical variations.

This method only provides information on the rock fabric as it is, i.e. that of the surface, without estimate its evolution during its burial.

Without the exceptional situation of the quarantine, more than 4 thin sections would be analyzed. We expected to apply this method to all our thin sections.

a) Crystallographic orientations

The EBSD analysis compiles the Euler angles for all pixels in a study area. From these and when the mineral phase is recognized, a wide combination of figures can be obtained. For example, the phase map in figure 11, which shows the distribution, proportions and arrangement of the minerals.

Figure 11A refers to sample BDC04, which is composed mainly of micas, amphiboles, titanites, epidotes and quartz. This fabric is, hence, close to that visible under the microscope (Fig. 6).

However, we can easily notice a poorly indexed phase. According to the microscopic observations, they are probably feldspar with variable chemistry, or inside them other minerals have recrystallized, making the structure more complex to detect. The same problem occurs with the RAB1904 section (Fig. 11C). The non-indexation seems to apply to a real undetected mineralogical phase and is not due to the surface section. One way to improve the indexation would be to resample the unconstrained portion of the section, even at a smaller sampling step. In contrast, the eclogitic sample (RAB1901A, Fig.11B) is well recognized and consistent with microscopic observations.

Other than phases map, following EBSD analyses, we obtain the Euler angles of each grains. It is therefore possible to make orientation maps of one or more minerals or to create pole figures. This kind of diagram are widely used to plot the CPO of a mineral in the coordinates of its sample. They function similarly to stereographic projections of faults and folds. Here the results are not detailed as they would be superfluous with the following ones, i.e. the associated Vp and VS velocities for each phase and the bulk rock.

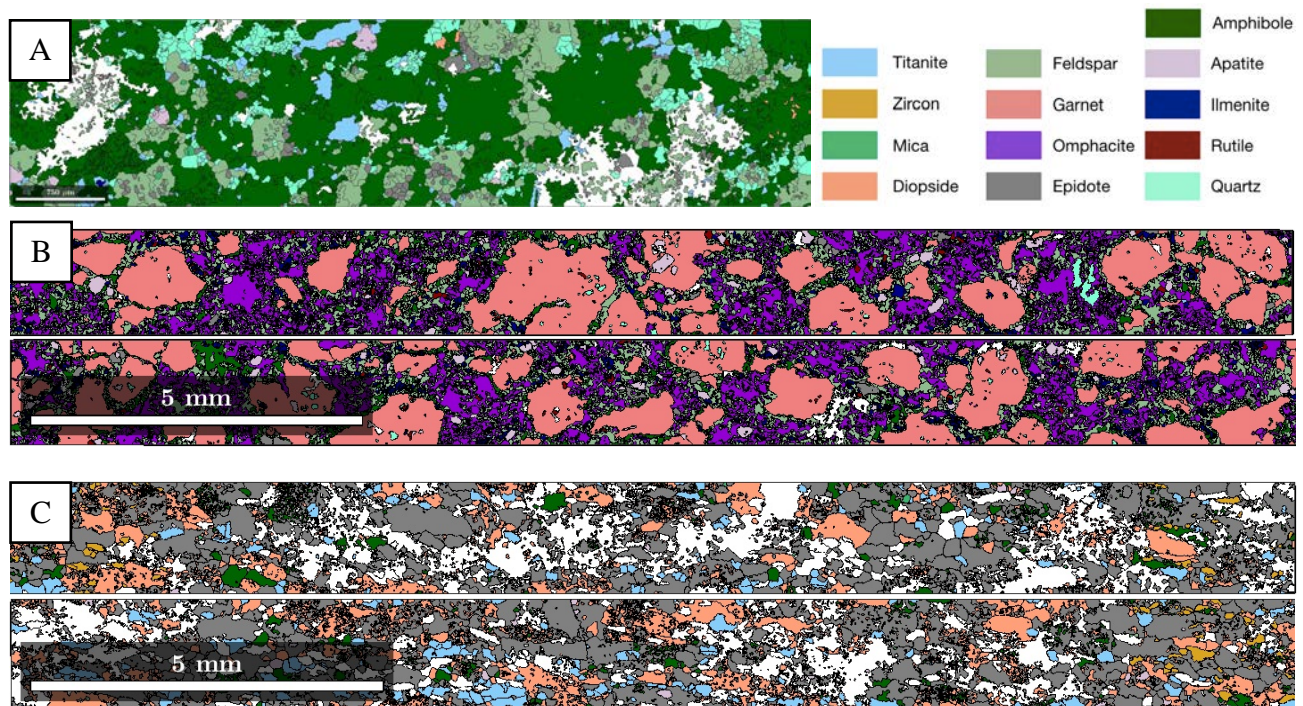


Figure 11: Phases maps of 3 on 4 samples analyzed via EBSD (A: BDC04, B: RAB1901A, C: RAB1904). Not indexed pixels are in white. RAB1901A and RAB1904 maps are continuous. Yet, for formatting reasons, they have been split into 2. The AN1907 phase map is not shown here, due to poor pixel indexing.

b) Seismic properties modeling from fabric

Figure 12 compares the P-wave seismic velocity and anisotropy results for the major minerals of 4 samples (an eclogite, RAB1901A and 3 amphiboles, RAB1904, BDC04 and AN1907), as well as the bulk rock.

For AN1907 sample, quartz, amphibole and mica are considered, they make up 80% of the rock. Quartz represents 39% of the rock and has a slight anisotropy (1,23%). Their velocities (around 6,2 km/s) are consistent with those of Almquist & Mainprice, 2017 (from 5,4 to 6,8 km/s). Mica (muscovite) has a much more obvious anisotropy (42%), but constitutes only 13% of the rock. Lastly, amphibole is in a greater proportions (28%) and with a significant anisotropy (14%). Thus, since it combines both proportions and fabric, it mainly drives the anisotropy of the total rock, even if we can observe the effect of mica too, at least in the shape of the anisotropy. This makes sense

with what we expected. In mafic lithologies, the minerals likely to develop a high enough anisotropy are amphiboles. Even if mica have this particularity, they are too scarce in these lithologies and occur rather in the felsic rocks. In contrast, the seismic velocities of the bulk rock (around 6,6 to 7,4 km/s) match with the average seismic velocities of the minerals (6,5, 6,2 and 8,2 km/s) and does not seem to be influenced by a single phase.

Regarding eclogite RAB1901A, more minerals are taken into account (felspath, garnet, amphibole, omphacite and diopside to get 93,7%). This time, although amphibole is almost as anisotropic as previously (from 14 to 12,3 %), it is much less present. Garnet is the dominant phase (51%), with a near-zero anisotropy (0,14%), which is consistent with its cubic crystallography. Its low anisotropy is explained by the low proportions of anisotropic minerals which, moreover, grow radially, in symplectite and thus on the retrograde path, based on microscopic observations. However, its velocities are too high to be realistic ($> 10,6$ km/s against 9 km/s from Lloyd et al., 2011). This is possibly due to the density and stiffness tensor values taken here, and should be further investigated.

Omphacite and diopside have also high seismic velocities (respectively 9,5 and 9 km/s). Omphacite values seem to be a bit too high regarding/according to those obtained by Bascou et al., 2001 (V_p max 9,37 km/s). Diopside's seismic velocities (around 9 km/s) are located in the upper range of those of Almqvist & Mainprice, 2017. Lastly, feldspar is the lowest velocity phase (6,35 km/s) and the second higher in proportions and anisotropy. Thus the resulting bulk rock has a shape of anisotropy close to that of the amphibole, but smoothed with the low values of the other phases.

RAB1904 (~ 90% represented) has a bulk rock pattern similar to AN1907, in the shape and values of the anisotropy but its minimum V_p is the maximum of the other. Since this sample is 70% amphibole, the resulting bulk rock is very strongly influenced by this phase, both in shape and anisotropic values and in seismic velocities.

Finally, as for the previous samples, BDC04 is influenced by amphiboles, but also by feldspars, which are present in large proportions, have a high anisotropy and the same shape as amphiboles.

IV. Discussion

A. Comparative impact of fabric and mineralogical proportions on seismic properties

1. The unmodified crust scenario

The processing of the EBSD data via MTEX led to different conclusions regarding P-wave velocities and anisotropies in the 3 chemical groups. These samples form the "unmodified crust" scenario of the study, if we consider that this rocks could be subjected without significant changes. Overall, amphibolites have low velocities and high anisotropies (about 12 %) and eclogite have high velocities and minimum anisotropy.

On one side, the amphibole has a strong impact on the anisotropy of the bulk rock, whether it is its shape or its value and whatever its proportion in the rock. Even if we have only one example of micas and amphiboles assemblage, in this one the anisotropy of the mica is so important, that they also govern the anisotropy of the rock. Contrary to what was initially thought, their impact in mafic rocks may not be so limited. Further study would obviously be necessary. One thing to do as well, would be to verify the reverse, that means the impact of amphiboles in felsic rocks, where mica is expected to dominate.

On other side, P-wave seismic velocities, resulting from the sum of amphibolite textures or a retrograde eclogitic, vary significantly (from 6,6 to 9,6 km/s). According to Solarino et al. 2018, a part of the upper crust has a velocity around 6,5 km/s, as well as the lower crust, while 9,6 km/s is close to those of the lithospheric mantle. Therefore, at depth, the seismic signature of the rocks,

with a seismic velocity similar to that of the crust, will be marked above all by their anisotropy. This is the case for AN1907. In contrast, RAB1901A, which is an eclogite, will not be detectable thanks to its almost zero anisotropy, but by a high contrast of velocity with the surrounding mantle, of generally lower velocities.

Therefore, if the alpine slab evolves from an amphibolitic lithology (AN1907) to an eclogitic lithology (RAB1901A), its seismic signature will first be seen by anisotropic contrasts, detectable via the receiver functions, then by velocity contrasts, via tomography.

However, thinking this way, we only taking account the mineralogical and fabric variations of the alpine slab, while we should consider those of the surrounding mantle too. Since only contrasts are detected, we have access to relative changes between the crust and the surrounding mantle, not to the absolute ones. Hence, anisotropic and velocities mantle variations has to be constrain, in order to compare it with the tomography and the receiver functions data. In this study, we considered the surrounding mantle as inert and we look at the changes generated in the alpine slab. The reverse reasoning should be used as well. We should apply this study to the mantle rocks, such as peridotite.

Similarly, since the retrograde minerals come from the exhumation path, and since we are concerned with the seismic properties of buried rocks, it would be interesting to subtract them from the high velocity eclogite (RAB1901A) and deduce the seismic velocities associated to the grt + omp assemblage, necessarily closer to the peak. Subtracting the mineral part of the retrograde path is conceivable since we are able to identify the different phases of mineralization, however, the retrograde part in the finished fabric of the rock is more difficult to identify.

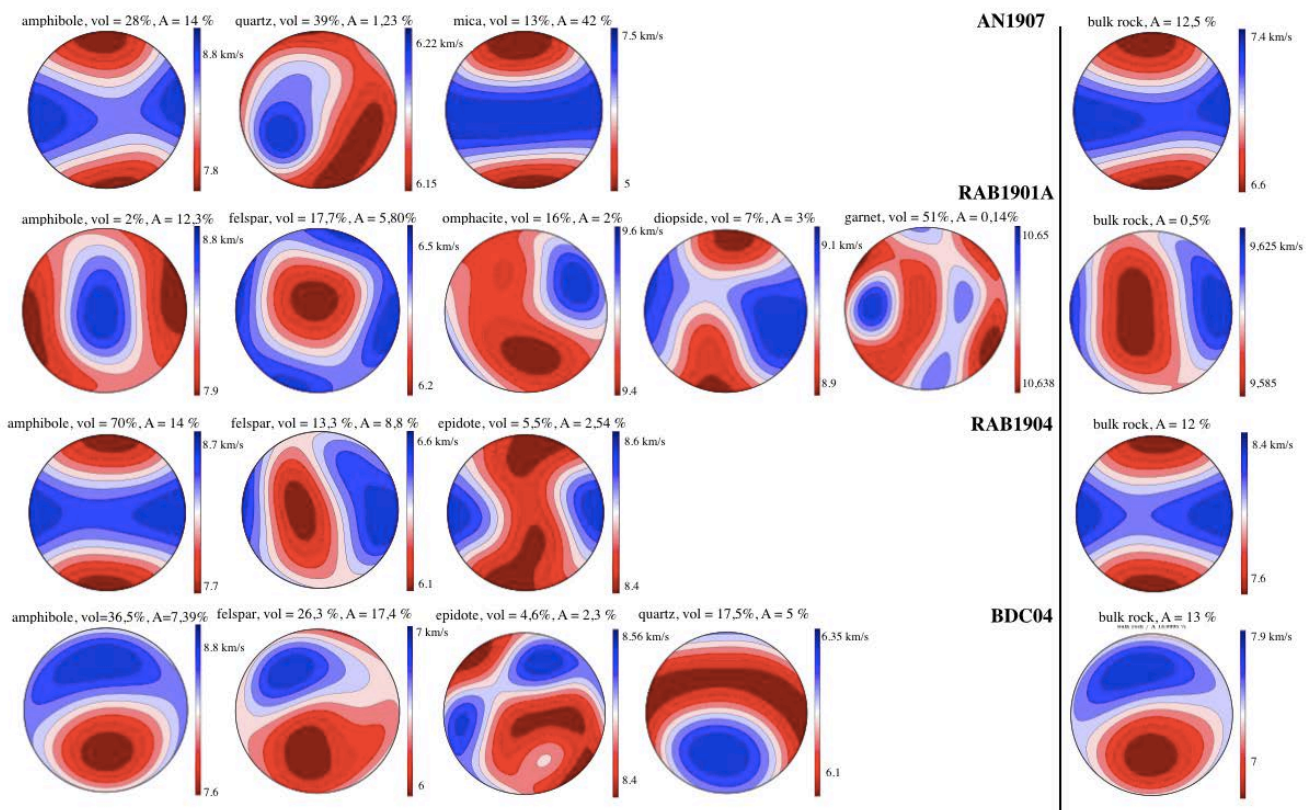


Figure 12: Synthesis of Vp and anisotropy modeling via MTEX, for the major minerals of the 4 samples analyzed at EBSD and for the resulting bulk rock. In red, Vp is lower than in blue. Amphibole is the common phase between all the samples.

2. The fully equilibrated crust at depth scenario

The thermodynamic modeling of the paragenesis during burial allows us to explore the "fully re-equilibrated crust at depth" scenario.

Based on thermodynamic modeling and the Abers & Hacker database, 2016, the seismic variations resulting from the variations of mineralogical assemblages were studied, in PT space. Wide knowledge of the elastic parameters of minerals (Lloyd et al., 2011, Almqvist & Mainprice 2017) allows the calculation of V_p , V_s and their anisotropies for an aggregate whose crystallographic proportions and orientations are known. Regarding the range of seismic velocity of P-waves, the mafic group seems to be more consistent with that from the tomography along the CIFALPS profile in Solarino et al. 2018.

However, this calculation takes into account neither the geometry of the phases (bedding, veins...) nor the effect of grain joints or micro-cracks which can increase or reduce the resulting anisotropy.

Moreover, these variations do not specify the pattern of seismic velocities along the PT path taken by the slab. Therefore, in figure 13, the variations of V_p as a function of depth are shown. In black are plotted the lower crust, constituting the alpine slab, from the tomographic profile of Solarino et al. 2018; those extracted from the Abers and Hacker models, for the mafic group, are in colors, according to the temperature gradient. It would seem that the alpine slab follow a temperature gradient close to 12°C up to 50 km, after which the seismic velocities in tomography are less well constrained. This graph also shows that variations in wave velocity as a function of depth and for given temperature gradients, is not linear but rather symmetrical. At a depth of 50km, the curves converge. As the input arguments are only mineralogical, one would have to associate these V_p with PT couples, and not only with z , to deduce the metamorphic reaction(s) responsible. Considering a gradient of 10 kbar for 30 km, at 50 km the pressure is about 1.6 GPa. The responsible phases could therefore be amphibole or feldspar, depending on the pseudosections (Fig.9A).

Another interesting graph would be to show the evolution of velocity and anisotropy values with increasing pressure-temperature conditions.

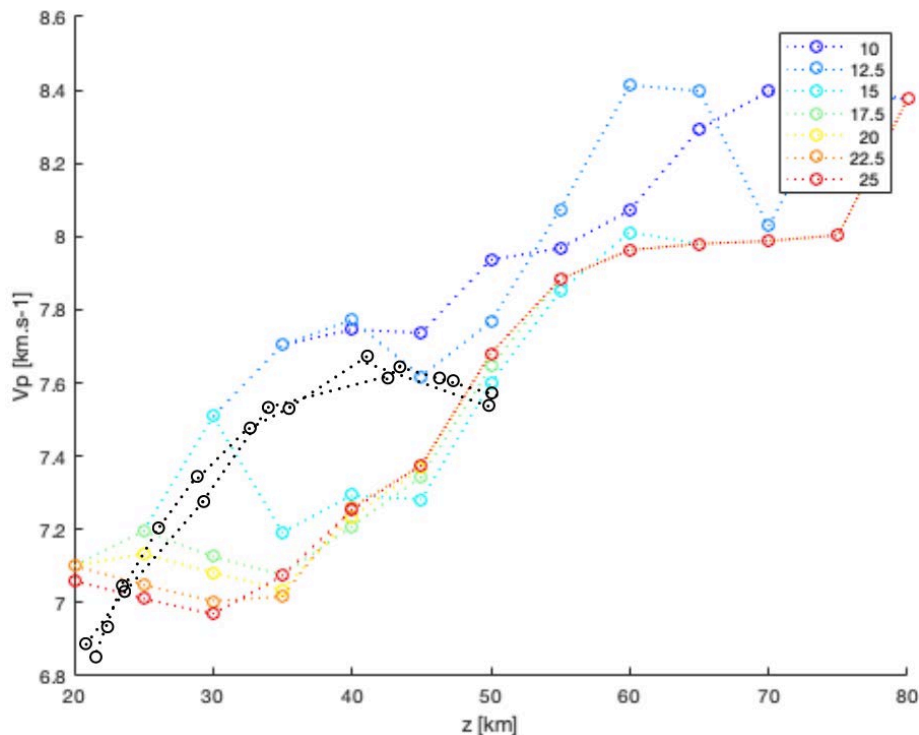


Figure 13: Variations of V_p with depth along the alpine slab (black dots) and according to different thermal gradients borrowed by the mafic group (color dots).

B. What is the petrological sensitivity of geophysical images?

There are sufficient ways to obtain the seismic properties of the rocks. However, the question of the representativity of the sample must be considered. The internship issue applies to the scale of the chain. It seeks to compare tomography data, whose imaged structures are of the order of a kilometer, with seismic properties deduced from samples, at a scale much smaller than the resolution of the geophysical images.

Therefore, we need to specify the degree of detail about the structure and nature of the rock that the geophysical images tell us. How complex are the geophysical images? Figure 14 represents blocks of increasing complexity in finite geometry. By interpreting these images to the maximum, can we only detect a petrological heterogeneity (as represented by the 1st block, fig. 14), a geometric heterogeneity (this is the 2nd block, fig. 14) or even an anisotropy in addition to a petrological heterogeneity and a dip (which corresponds to the last block, fig. 14)?

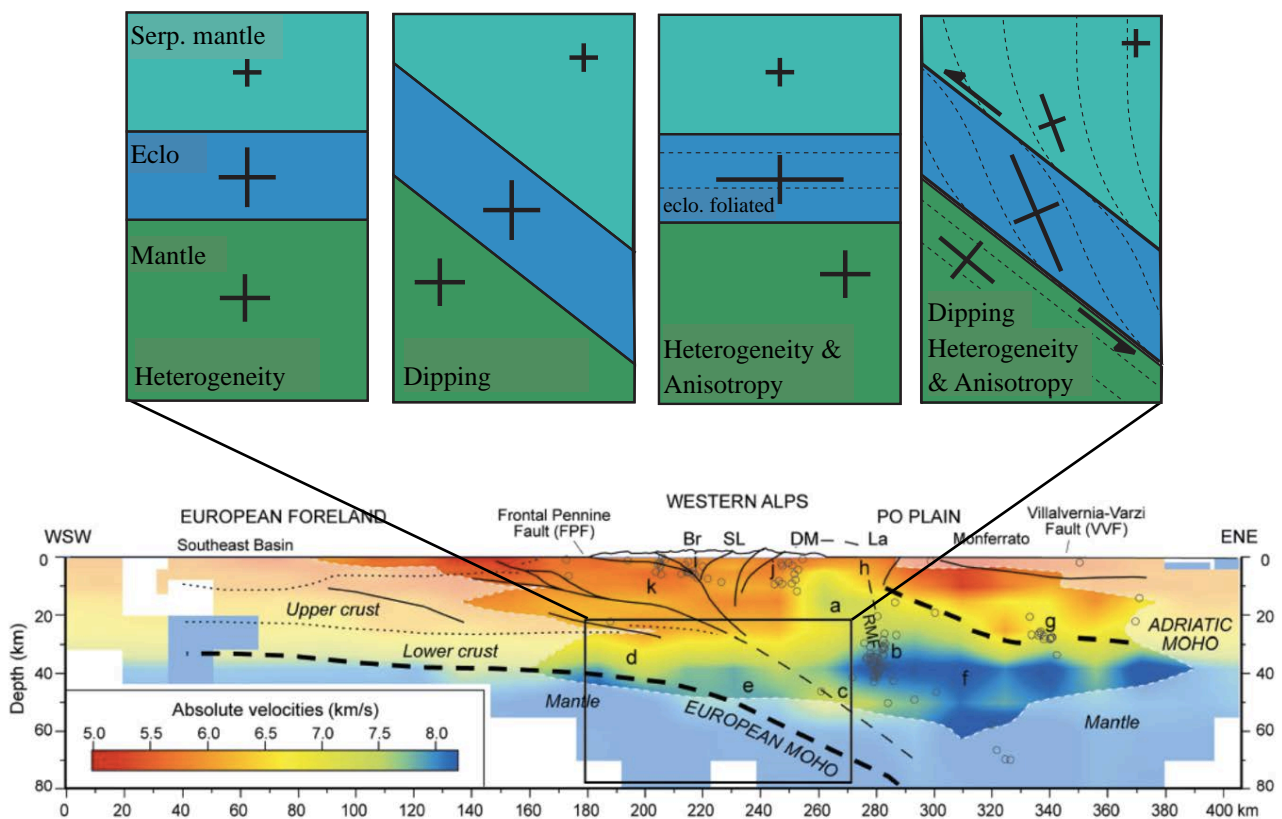


Figure 14: Complexity of the nature and structure of a rock in comparison with tomographic images. The blocks are all made up of a serpentine mantle at the top, then an eclogitized zone in blue and a homogeneous mantle in green. They represent examples of increasingly complex finished geometries. The figure asks about the level of detail detectable in tomographic images, such as this section of the Western Alps, from Solarino et al. 2018.

C. What next? Synthetic geophysical signature of hecto- to kilometer scale structures

To overcome this issue, modeled seismic properties must be combined with direct sample measurements. Kern's press makes it possible, using the ultrasonic pulse emission technique through the samples. Since seismic velocities are closely related to elastic and geomechanical properties, seismic properties of the rock can be deduced from this propagation. These measures could be supported by modeling.

First, thermodynamic models, in order to predict the metamorphic reactions for each lithology and to evaluate their impact during burial. The destabilization of plagioclase in clinopyroxene and the

growth of garnet are often seen as first order reactions during eclogitization. One thus expects to observe its transformations in geophysics. However, the destabilization of phengite in felsic rocks and the transient growth of amphibole or epidote in intermediate rocks could also cause a significant contrast, with variable ray incidence dependencies (Barberini et al., 2007, Fujimoto et al., 2010). Then, dynamic wave propagation modeling could complement direct measurements of seismic properties (Zhong et al. 2014). It takes into account phase geometry and micro-structures, and even models the response of aggregates to variable frequency signals. Thanks to it, the results from EBSD measurements of crystal textures and orientations could be compared.

The next step consists in layering the rocks into hecto- to kilometre-scale structures representative of the major contacts and producing synthetics of their geophysical signature. These blocks stack effects of contrast, geometry and anisotropy. In order to detect the petrological sensitivity of the geophysical images, each of these effects should be decomposed into easier blocks where each effect can be estimated on the effects of the equivalent effective environment.

A next step is scaling up to the higher order (10 km), this time to reproduce the data at the same scale as the seismological profiles, knowing that a given scale heterogeneity will result in an anisotropy at the higher integration scale.

Finally, even if the basic lithologies, on which I am currently working, are good candidates for those in depth, constituting the lower crust, other lithologies are proposed in the bibliography (granulites and felsic eclogites, serpentinized mantle or UHP slivers, Solarino et al., 2018), which should be tested in order to answer the question correctly.

V. Conclusion

The approach undertaken during this internship is complementary to that of the geophysicists since it is direct: from rock samples, we characterize their seismic properties. Whereas geophysicists proceed indirectly: they deduce the seismic properties of rocks from the velocity of seismic waves. Thus, starting from the rock, we could greatly contribute to improve the interpretation of geophysical images.

The objective of this study was to determine which lithologies, rebalanced in which proportions and bearing which fabric are likely to generate the signals recorded by geophysics. The lack of data and measurements due to confinement does not allow to answer this question completely.

However, we can already claim that the transition from amphibolitic to eclogitic facies is responsible for a velocity jump (from 7.4 km/s to 8.2 km/s in mafic rocks). Looking at the modeled seismic properties of rocks and minerals from their fabric, this jump is mainly explained by the loss of amphiboles and the occurrence of garnets, whose anisotropy is almost zero.

Finally, direct measurements of V_p and V_s tensors under HT and HP conditions should be included, and wave propagation through synthetic heterogenic sequences based on field lithostratigraphic logs should be modeled in order to properly address the upscaling necessary for the problem, the purpose of this project being, among other things, to determine the petrological sensitivity of the geophysical images.

VI. Acknowledgments

I would like to thank Loïc Labrousse for offering me this internship, through which he also offers me a thesis. Your investment, even remotely, allowed me to work in a cozy environment and your judicious advices have contributed to guiding me and feeding my reflection. Many thanks to Alexis Plunder and Jérôme Bascou for having followed my internship in these conditions and Alexis for your contribution in the field. I look forward to more interacting together during the thesis. Thanks to Jean Baptiste Jacob for coming with me on the field.

I must also greatly thank Omar Boudouma, without whom the EBSD measures would not have been possible. Thanks also to Benoit Caron and Benoit Dubacq for their support in my ICP-OES measurements.

VII. References

- Abers, G.A., Hacker, B.R., 2016. A MATLAB toolbox and Excel workbook for calculating the densities, seismic wave speeds, and major element composition of minerals and rocks at pressure and temperature: MATLAB AND EXCEL TOOLS FOR ROCK WAVE SPEEDS. *Geochem. Geophys. Geosyst.* 17, 616–624. <https://doi.org/10.1002/2015GC006171>
- Alder, C., Bodin, T., Ricard, Y., Capdeville, Y., Debayle, E., Montagner, J.P., 2017. Quantifying seismic anisotropy induced by small-scale chemical heterogeneities. *Geophysical Journal International* 211, 1585–1600. <https://doi.org/10.1093/gji/ggx389>
- Almqvist, B.S.G., Mainprice, D., 2017. Seismic properties and anisotropy of the continental crust: Predictions based on mineral texture and rock microstructure: SEISMIC PROPERTIES OF THE CRUST. *Rev. Geophys.* 55, 367–433. <https://doi.org/10.1002/2016RG000552>
- Barberini, V., Burlini, L., Zappone, A., 2007. Elastic properties, fabric and seismic anisotropy of amphibolites and their contribution to the lower crust reflectivity. *Tectonophysics* 445, 227–244. <https://doi.org/10.1016/j.tecto.2007.08.017>
- Barruol, G., Mainprice, D., 1993. A quantitative evaluation of the contribution of crustal rocks to the shear-wave splitting of teleseismic SKS waves. *Physics of the Earth and Planetary Interiors* 78, 281–300.
- Bascou, J., Barruol, G., Vauchez, A., Mainprice, D., Egydio-Silva, M., 2001. EBSD-measured lattice-preferred orientations and seismic properties of eclogites. *Tectonophysics* 342, 61–80. [https://doi.org/10.1016/S0040-1951\(01\)00156-1](https://doi.org/10.1016/S0040-1951(01)00156-1)
- Bascou, J., Doucet, L.S., Saumet, S., Ionov, D.A., Ashchepkov, I.V., Golovin, A.V., 2011. Seismic velocities, anisotropy and deformation in Siberian cratonic mantle: EBSD data on xenoliths from the Udachnaya kimberlite. *Earth and Planetary Science Letters* 304, 71–84. <https://doi.org/10.1016/j.epsl.2011.01.016>
- Capdeville, Y., Zhao, M., Cupillard, P., 2015. Fast Fourier homogenization for elastic wave propagation in complex media. *Wave Motion* 54, 170–186. <https://doi.org/10.1016/j.wavemoti.2014.12.006>
- de Capitani, C., Petrakakis, K., 2010. The computation of equilibrium assemblage diagrams with Theriak/Domino software. *American Mineralogist* 95, 1006–1016. <https://doi.org/10.2138/am.2010.3354>
- Faccenda, M., Ferreira, A.M.G., Tisato, N., Lithgow-Bertelloni, C., Stixrude, L., Pennacchioni, G., 2019. Extrinsic Elastic Anisotropy in a Compositionally Heterogeneous Earth's Mantle. *J. Geophys. Res. Solid Earth* 124, 1671–1687. <https://doi.org/10.1029/2018JB016482>
- Frederiksen, A.W., Bostock, M.G., 2000. Modelling teleseismic waves in dipping anisotropic structures. *Geophysical Journal International* 141, 401–412. <https://doi.org/10.1046/j.1365-246x.2000.00090.x>
- Fujimoto, Y., Kono, Y., Hirajima, T., Kanagawa, K., Ishikawa, M., Arima, M., 2010. P-wave velocity and anisotropy of the lawsonite and epidote blueschists: constraints on water transportation along subduction oceanic crust. *Physics of the Earth and Planetary Interiors* 183, 219–228. <https://doi.org/10.1016/j.pepi.2010.09.003>
- Hacker, D.B., Biek, R.F., Rowley, P.D., 2014. Catastrophic emplacement of the gigantic Markagunt gravity slide, southwest Utah (USA): Implications for hazards associated with sector collapse of volcanic fields. *Geology* 42, 943–946. <https://doi.org/10.1130/G35896.1>

- Kern, H., Liu, B., Popp, T., 1997. Relationship between anisotropy of P and S wave velocities and anisotropy of attenuation in serpentinite and amphibolite. *J. Geophys. Res.* 102, 3051–3065. <https://doi.org/10.1029/96JB03392>
- Lloyd, G.E., Butler, R.W.H., Casey, M., Tatham, D.J., Mainprice, D., 2011. Constraints on the seismic properties of the middle and lower continental crust. Geological Society, London, Special Publications 360, 7–32. <https://doi.org/10.1144/SP360.2>
- Malusà, M.G., Wang, J., Garzanti, E., Liu, Z.-C., Villa, I.M., Wittmann, H., 2017. Trace-element and Nd-isotope systematics in detrital apatite of the Po river catchment: Implications for provenance discrimination and the lag-time approach to detrital thermochronology. *Lithos* 290–291, 48–59. <https://doi.org/10.1016/j.lithos.2017.08.006>
- Motra, H.B., Zertani, S., 2018. Influence of loading and heating processes on elastic and geomechanical properties of eclogites and granulites. *Journal of Rock Mechanics and Geotechnical Engineering* 10, 127–137. <https://doi.org/10.1016/j.jrmge.2017.11.001>
- Nabelek, J., Hetenyi, G., Vergne, J., Sapkota, S., Kafle, B., Jiang, M., Su, H., Chen, J., Huang, B.-S., Team, t. H.-C., 2009. Underplating in the Himalaya-Tibet Collision Zone Revealed by the Hi-CLIMB Experiment. *Science* 325, 1371–1374. <https://doi.org/10.1126/science.1167719>
- Nicolas, A., Polino, R., Hirn, A., Nicolich, R., and ECORS-CROP working group, 1990. ECORS-CROP traverse and deep structure of the western Alps: a synthesis. *Memoire de la Société Géologique de France* n°156, pp 15-27.
- Piromallo, C., Faccenna, C., 2004. How deep can we find the traces of Alpine subduction? *Geophysical research letters*, 31. L06605. <https://doi:10.1029/2003GL019288>.
- Rondenay, S., Abers, G.A., van Keken, P.E., 2008. Seismic imaging of subduction zone metamorphism. *Geol* 36, 275. <https://doi.org/10.1130/G24112A.1>
- Schmid, S.M., Fgenschuh, B., Kissling, E., Schuster, R., 2004. Tectonic map and overall architecture of the Alpine orogen. *Eclogae geol. Helv.* 97, 93–117. <https://doi.org/10.1007/s00015-004-1113-x>
- Schneider, F.M., Yuan, X., Schurr, B., Mechie, J., Sippl, C., Haberland, C., Minaev, V., Oimahmadov, I., Gadoev, M., Radjabov, N., Abdybachaev, U., Orunbaev, S., Negmatullaev, S., 2013. Seismic imaging of subducting continental lower crust beneath the Pamir. *Earth and Planetary Science Letters* 375, 101–112. <https://doi.org/10.1016/j.epsl.2013.05.015>
- Schulte-Pelkum, V., Monsalve, G., Sheehan, A., Pandey, M.R., Sapkota, S., Bilham, R., Wu, F., 2005. Imaging the Indian subcontinent beneath the Himalaya. *Nature* 435, 1222–1225. <https://doi.org/10.1038/nature03678>
- Shapiro, N.M., Ritzwoller, M.H., 2004. Thermodynamic constraints on seismic inversions. *Geophysical Journal International* 157, 1175–1188. <https://doi.org/10.1111/j.1365-246X.2004.02254.x>
- Solarino, S., Malusà, M.G., Eva, E., Guillot, S., Paul, A., Schwartz, S., Zhao, L., Aubert, C., Dumont, T., Pondrelli, S., Salimbeni, S., Wang, Q., Xu, X., Zheng, T., Zhu, R., 2018a. Mantle wedge exhumation beneath the Dora-Maira (U)HP dome unravelled by local earthquake tomography (Western Alps). *Lithos* 296–299, 623–636. <https://doi.org/10.1016/j.lithos.2017.11.035>
- Solarino, S., Malusà, M.G., Eva, E., Guillot, S., Paul, A., Schwartz, S., Zhao, L., Aubert, C., Dumont, T., Pondrelli, S., Salimbeni, S., Wang, Q., Xu, X., Zheng, T., Zhu, R., 2018b. Mantle wedge exhumation beneath the Dora-Maira (U)HP dome unravelled by local earthquake tomography (Western Alps). *Lithos* 296–299, 623–636. <https://doi.org/10.1016/j.lithos.2017.11.035>

- Very-high-pressure metamorphism in the western Alps: implications for subduction of continental crust, 1987. . *Phil. Trans. R. Soc. Lond. A* 321, 183–197. <https://doi.org/10.1098/rsta.1987.0010>
- Whitney, D.L., Evans, B.W., 2010. Abbreviations for names of rock-forming minerals. *American Mineralogist* 95, 185–187. <https://doi.org/10.2138/am.2010.3371>
- Yuan, X., Sobolev, S.V., Kind, R., Oncken, O., Bock, G., Asch, G., Schurr, B., Graeber, F., Rudloff, A., Hanka, W., Wylegalla, K., Tibi, R., Haberland, Ch., Rietbrock, A., Giese, P., Wigger, P., Röwer, P., Zandt, G., Beck, S., Wallace, T., Pardo, M., Comte, D., 2000. Subduction and collision processes in the Central Andes constrained by converted seismic phases. *Nature* 408, 958–961. <https://doi.org/10.1038/35050073>
- Zertani, S., Vrijmoed, J.C., Tilmann, F., John, T., Andersen, T.B., Labrousse, L., 2020. P-wave anisotropy caused by partial eclogitization of descending crust demonstrated by modeling effective petrophysical properties. *G³*, 21(6). <https://doi.org/10.1029/2019GC008906>
- Zertani, S., John, T., Tilman, F., Mitra, H.B., Keppler, R., Andersen, T.B., Labrousse, L., 2019. Modification oh the seismic properties of subducting continental crust by eclogitization and deformation processes. *JGR Solid Earth*, 124(9), 9731-9754. <https://doi.org/10.1029/2019JB017741>
- Zertani, S., Labrousse, L., John, T., Andersen, T.B., Tilmann, F., 2019. The interplay of eclogitization and deformation during deep burial of the lower crust- a case study from the Bergen Arc (Western Norway). *Tectonics*, 38(3), 898-915.
- Zhang, Z., Wang, Y., Houseman, G.A., Xu, T., Wu, Z., Yuan, X., Chen, Y., Tian, X., Bai, Z., Teng, J., 2014. The Moho beneath western Tibet: Shear zones and eclogitization in the lower crust. *Earth and Planetary Science Letters* 408, 370–377. <https://doi.org/10.1016/j.epsl.2014.10.022>
- Zhao, L., Paul, A., Guillot, S., Solarino, S., Malusà, M.G., Zheng, T., Aubert, C., Salimbeni, S., Dumont, T., Schwartz, S., Zhu, R., Wang, Q., 2015. First seismic evidence for continental subduction beneath the Western Alps. *Geology* 43, 815–818. <https://doi.org/10.1130/G36833.1>
- Zhong, X., Frehner, M., Kunze, K., Zappone, A., 2014. A novel EBSD-based finite-element wave propagation model for investigating seismic anisotropy: Application to Finero Peridotite, Ivrea-Verbano Zone, Northern Italy. *Geophys. Res. Lett.* 41, 7105–7114. <https://doi.org/10.1002/2014GL060490>

VIII. Appendix 1 - Hackers, QAFP and AFM diagrams

